JGR Atmospheres

RESEARCH ARTICLE
10.1029/2023JD039081

# Effects of Wind Shear and Aerosol Conditions on the Organization of Precipitating Marine Stratocumulus Clouds

**Jong-Hoon Jeong**[1,2], **Mikael K. Witte**[1,2,3], **and Mark Smalley**[1,2]

[1]Joint Institute for Regional Earth System Science and Engineering, University of California, Los Angeles, CA, USA, [2]Jet Propulsion Laboratory, California Institute of Technology, Pasadena, CA, USA, [3]Department of Meteorology, Naval Postgraduate School, Monterey, CA, USA

**Key Points:**

- Cloud droplet number concentration dominates vertical shear in determining the cellular cloud organization of idealized marine stratocumulus
- A stronger wind shear leads to a reduced cloud fraction associated with cloud thinning compared to cases with weaker shear
- Intermediate $N_d$ simulations with negligible surface precipitation produce cold pools with comparable intensity as a low $N_d$ configuration

**Supporting Information:**

Supporting Information may be found in the online version of this article.

**Correspondence to:**

J.-H. Jeong,
jeongjh737@gmail.com

**Citation:**

Jeong, J.-H., Witte, M. K., & Smalley, M. (2023). Effects of wind shear and aerosol conditions on the organization of precipitating marine stratocumulus clouds. *Journal of Geophysical Research: Atmospheres*, *128*, e2023JD039081. https://doi.org/10.1029/2023JD039081

Received 14 APR 2023
Accepted 22 NOV 2023

**Author Contributions:**

**Conceptualization:** Jong-Hoon Jeong, Mikael K. Witte
**Formal analysis:** Jong-Hoon Jeong
**Funding acquisition:** Mikael K. Witte, Mark Smalley
**Investigation:** Mikael K. Witte, Mark Smalley
**Methodology:** Jong-Hoon Jeong
**Project Administration:** Mikael K. Witte, Mark Smalley
**Supervision:** Mikael K. Witte, Mark Smalley
**Validation:** Mikael K. Witte, Mark Smalley
**Visualization:** Jong-Hoon Jeong
**Writing – original draft:** Jong-Hoon Jeong
**Writing – review & editing:** Jong-Hoon Jeong, Mikael K. Witte, Mark Smalley



**Abstract** This study examines how wind shear affects precipitating marine stratocumulus clouds under different cloud droplet number concentrations ($N_d$). We performed a series of large eddy simulations (LES) of nocturnal marine stratocumulus clouds using Cloud Model 1 (CM1). The simulations show that $N_d$ is the dominant factor for cloud cellular organization in this cloud regime rather than wind shear. Low $N_d$ characterizes the open cellular structure with a high in-cloud liquid water path (LWP). When wind shear is increased, the cloud fraction tends to decrease along with LWP, suggesting the cloud top region is significantly influenced by the entrainment and mixing of dry air from the free troposphere. We also examine cold pools in open and closed cellular clouds. Open-cell clouds produce larger and deeper cold pools compared to closed-cell clouds. Interestingly, cold pools can exist without surface precipitation and are produced by evaporation of light precipitation (drizzle) below the cloud base with weak downdrafts. The evaporation of raindrops and drizzle play an important role in initiating new convection, particularly where colliding outflows occur downstream of the cloud. This secondary convection contributes to the development and maintenance of the cloud cellular organization and formation.

**Plain Language Summary** Low altitude clouds cover a wide area of the Earth's atmosphere and play an important climatic role by reflecting sunlight back to space, thereby having been the topic of decades of study via observation and numerical simulation. This study uses high-resolution weather simulations to understand the influence of the winds and tiny particles on subtropical low clouds. We find that the tiny particles largely affect the cellular cloud organization (e.g., broken and unbroken clouds). When the wind near the surface is much weaker than wind above the surface, the cloud amount and thickness are decreased via mixing of the dry air at the cloud top. In addition, the different cloud organizations produced different cold pockets of dense air near the surface. The cold air resulting from broken clouds helps to initiate a new cloud downstream, and convection upstream of the unbroken cloud is enhanced by the cold air outflow.

## 1. Introduction

Stratocumulus (Sc) clouds are frequently observed over the ocean and have a profound effect on Earth's radiation budget due to their large coverage (Wood, 2012). The Sc clouds exhibit regular patterns on the mesoscale (20–200 km; Orlanski, 1975) organizations known as open-cellular (broken) and closed-cellular (unbroken) clouds (Wood & Hartmann, 2006). Since these two cellular patterns present distinct cloud morphology and coverage, they reflect different amounts of incoming solar radiation back to space (known as the negative shortwave cloud radiative effect; Hartmann & Short, 1980). Therefore, the net radiative effects are also different because the closed-cell clouds have a higher scene albedo with a larger cloud fraction than the open-cell clouds (Feingold et al., 2016). However, the representation of these low cloud morphologies in the current global circulation model (GCM) remains a challenge (Bony & Dufresne, 2005; Schneider et al., 2017), because the small scales of these cloud processes cannot explicitly be resolved, and their subgrid-scale variabilities need to be parameterized (Golaz et al., 2002; Morrison & Gettelman, 2008; Siebesma et al., 2007).

One of the primary causes of uncertainty in Global Climate Model (GCM) predictions, among other factors, is the subgrid-scale variability of aerosol-cloud interactions involving microphysical and radiative processes (Pawlowska & Brenguier, 2003; Seinfeld et al., 2016). This uncertainty arises from complex cloud macrophysical and microphysical responses to aerosols (Li et al., 2011; Stevens & Feingold, 2009). Consequently, the current GCMs are not able to fully represent the complexity of aerosol-cloud interactions. For instance, aerosols

serve as cloud condensation nuclei (CCN), and their presence can either increase or decrease cloud amount, depending on factors such as aerosol size distribution and concentration. Moreover, aerosols can exert influence over the microphysical characteristics of Sc clouds, as precipitation processes can impact aerosol concentrations, subsequently affecting the microphysics of Sc clouds. In a precipitating boundary layer, the aerosol size distribution and concentration can be modified by collision and coalescence processes associated with drizzle or precipitation in the subcloud layer, resulting in complex feedbacks between CCN, clouds, precipitation, and cloud morphology.

Large-eddy simulation (LES) modeling can resolve small-scale processes (<1 km) associated with aerosol-cloud interactions, allowing more accurate simulations of aerosol properties and their effects on Sc cloud organizations. Wang and Feingold (2009a) simulated the open- and closed-cellular clouds with a very large aerosol perturbation. They conducted experiments with three different cloud droplet number concentrations ($N_d$) of 65, 150, and 500 $cm^{-3}$ to investigate the impact of aerosol-cloud interactions on the evolution of open- and closed-cellular cloud structures. Their findings revealed that simulation with low $N_d$ produced the open-cellular cloud structure characterized by a relatively high amount of precipitation. This precipitation played a crucial role in generating dynamic response (e.g., turbulence) through enhanced evaporative cooling, ultimately contributing to the formation of cellular cloud organization. Similarly, Glassmeier and Feingold (2017) simulated a case of Sc clouds, exploring their geometric structure and self-organization by modulating the number of cloud droplets. They found that Sc clouds exhibit a network structure composed of links (line structures) and nodes (intersections of links), shedding light on the intricate organization of these clouds. Furthermore, a recent study performed Lagrangian cloud microphysics that can represent explicit aerosol activation, scavenging, and processing by tracking cloud-borne aerosol in super-droplets (Chandrakar et al., 2022). They simulated the closed-to-open cell transition by modulating aerosol size distribution and concentration. The study emphasized the significant role of precipitation development in driving the transition from closed-cell to open-cell cloud configuration.

Here, we consider that vertical wind shear (hereafter "wind shear") in the boundary layer may also play a role in convection and cloud evolution. Numerous studies demonstrate the impacts of wind shear on deep convective cloud dynamics (Chakraborty et al., 2016; Houze, 2018; Peters et al., 2022) and microphysical processes (Fan et al., 2009; Khain et al., 2005). Several studies have also discussed the effect of wind shear on shallow cumulus clouds using LES. For instance, Yamaguchi et al. (2019) show that wind shear results in tilting clouds and spreading cloud tops horizontally, which increases cloud fraction and evaporation aloft. Helfer et al. (2020) find that wind shear influences the depth and characteristics of shallow cumulus convection, and therefore the cloud structure of the trade-wind layer. In contrast, many fewer studies have discussed the simultaneous influence of both wind shear and aerosol perturbations on Sc clouds. Recently, Zamora Zapata et al. (2021) found that Sc clouds had lower cloud fraction and liquid water path (LWP) with increasing surface and top wind shear, but they did not explore covariability of wind shear effects with microphysical factors.

As mentioned earlier, drizzle and precipitation in the subcloud layer can significantly influence the transition from closed-cell to open-cell clouds. When raindrops fall into unsaturated air, they can evaporate, causing a descent of cold air to the surface. This near-surface cold air then spreads horizontally, displacing the surrounding warmer air and forming cold pools. While many studies have focused on cold pools in deep convective clouds, recent research has highlighted the importance of cold pools in Sc clouds, particularly those with relatively smaller precipitation drop sizes (e.g., Wood, 2005b) and drizzle that evaporates in the subcloud layer (e.g., Wood, 2005a). Wang and Feingold (2009a) emphasized the critical role of evaporative cooling from precipitation in the formation and evolution of open-cellular clouds. Feingold et al. (2010) revealed that when the boundaries of cold pools from adjacent cells collide, the resulting surface convergence can result in updrafts and the generation of new clouds. Additionally, Yamaguchi et al. (2017) demonstrated that drizzle and precipitation are important factors that cause boundary layer decoupling and contribute to the transition from Sc to cumulus cloud structures.

The present study investigates how wind shear affects precipitating marine Sc clouds under different aerosol conditions using LES with constant wind shear and $N_d$ varying between simulations. The rest of the paper is organized as follows. Section 2 presents the case description and LES setup for the wind shear experiments under different aerosol conditions. The results and discussion are presented in Section 3, which is split into two parts. First, we discuss the effect of $N_d$ on cellular cloud organizations using object-based cloud classification. Second, the effects of wind shear and cold pools on the cloud structures are discussed. Section 4 contains the conclusions of this work.

## 2. Methods and Simulations

### 2.1. Model Configuration

An idealized case study of nocturnal marine stratocumulus observed during the second research flight (RF02) of the Second Dynamics and Chemistry of Marine Stratocumulus field study (DYCOMS-II) field campaign (Ackerman et al., 2009) is simulated using Cloud Model 1 (CM1; Bryan & Fritsch, 2002), version 20.2 (cm1r20.2). The domain has 1,000 × 1,000 grid points in the horizontal and horizontal grid spacing $\Delta x = \Delta y = 50$ m. The simulated domain of $50 \times 50$ km$^2$ allows for the development of mesoscale cloud organization (de Roode et al., 2004). The vertical grid contains 96 levels. The vertical grid spacing stretched from 2.5 m near the surface up to the mid-boundary layer (374 m) with a maximum layer thickness of 25 m. It then contracts again from 25 to 5 m between 450 m and the inversion height (795 m) within a zone of constant $dz = 5$ m spanning approximately 125 m around the mean inversion height, and finally stretches again until it reaches the model's top at 1.5 km, with spacing of approximately 80 m (see $dz$ profile in Figure S1 of the Supporting Information S1). The model is integrated for 12 hr to allow sufficient time for cloud organization to develop and mature. Doubly periodic conditions are applied at lateral boundaries. The radiative forcing is parameterized by a simple model of the net longwave radiative flux following Stevens et al. (2005). Subgrid-scale mixing uses the 1.5-order TKE-based scheme of Deardorff (1980). A Klemp-Wilhelmson time-splitting vertically implicit pressure solver is used, with an adaptive time step of at most 5 s following a Runge–Kutta scheme (Klemp & Wilhelmson, 1978). A fifth-order scheme with implicit diffusion is used to integrate the horizontal and vertical advection of velocities and scalars, with a weighted essentially nonoscillatory (WENO) scheme applied at the final Runge-Kutta time step to the advection of momentum and scalars (Wicker & Skamarock, 2002). Shi et al. (2018) noted that Sc clouds are highly sensitive to the advection scheme and many LES models tend to produce unrealistically thin cloud layers and a decoupled boundary layer structure due to numerical diffusion of warm, dry air across sharp temperature inversions. To address this issue, they suggested the use of fifth-order WENO scheme for the advection of both momentum and scalars, as it resulted in high-fidelity simulations compared to other numerical schemes. When employing the fifth-order WENO scheme for both momentum and scalars, the simulation demonstrated improved representation of entrainment in the cloud-top region and reduced the numerical diffusion. The Morrison double-moment scheme is used to emulate microphysical processes with assumed constant cloud drop number concentration (Morrison et al., 2005, 2009). In the Morrison double-moment scheme, autoconversion of cloud droplets and accretion of cloud droplets by rain follow the scheme developed by Khairoutdinov and Kogan (2000), which was originally designed for LES of marine stratocumulus clouds.

### 2.2. Case Description and Experimental Design

The standard simulation setup follows the GEWEX Cloud System Study (GCSS) model intercomparison based on an idealization of nocturnal aircraft measurements during RF02 of DYCOMS-II over the northeast Pacific off the coast of California. The flight observed heavily drizzling open cells amid a deck of closed-cell marine Sc that was drizzling lightly (vanZanten & Stevens, 2005). The case also has a tendency to transition from the closed- to open-cell regime when $N_d$ is sufficiently low (e.g., 15 cm$^{-3}$; Feingold et al., 2015; Glassmeier & Feingold, 2017). Figure 1 shows the initial atmospheric profiles of temperature, moisture, and winds following Ackerman et al. (2009) and Savic-Jovcic and Stevens (2008). The liquid-water potential temperature ($\theta_l$) was initialized to 288.3 K in the boundary layer, increasing to 303.9 K by 1,500 m height (Figure 1a). The inversion height was 795 m. The total water mixing ratio ($q_t$) was initialized at 9.45 g kg$^{-1}$ in the boundary layer, decreasing to 5.0 g kg$^{-1}$ in the free troposphere (Figure 1b). The zonal component wind was 3 m s$^{-1}$ at the surface and linearly increased with height at a rate of 4.3 m s$^{-1}$ km$^{-1}$ (black line in Figure 1c). The meridional wind was −9 m s$^{-1}$ at the surface and decreased with height at a rate of 5.6 m s$^{-1}$ km$^{-1}$ (black line in Figure 1d). The simulation has a uniform sea surface temperature (SST) fixed at 299.28 K.

To investigate the impact of wind shear and aerosol conditions on the evolution of cellular cloud organization, a total of nine numerical simulations were conducted with (a) three different vertical wind profiles and (b) three different $N_d$ values as a proxy for different aerosol loadings (Wang & Feingold, 2009a, 2009b; Zhou et al., 2017). In general, elevated aerosol concentrations enhance CCN concentrations and correspondingly the density of $N_d$ within the cloud (Ghan et al., 2001). For the wind shear experiments, the simulations labeled with 0X, 1X, and 1.5X correspond to multiplicative factors of 0, 1, and 1.5 applied to the wind shear of the standard case (black lines in Figures 1c and 1d). All wind profiles featured unidirectional southwest-to-southeast shear. Although

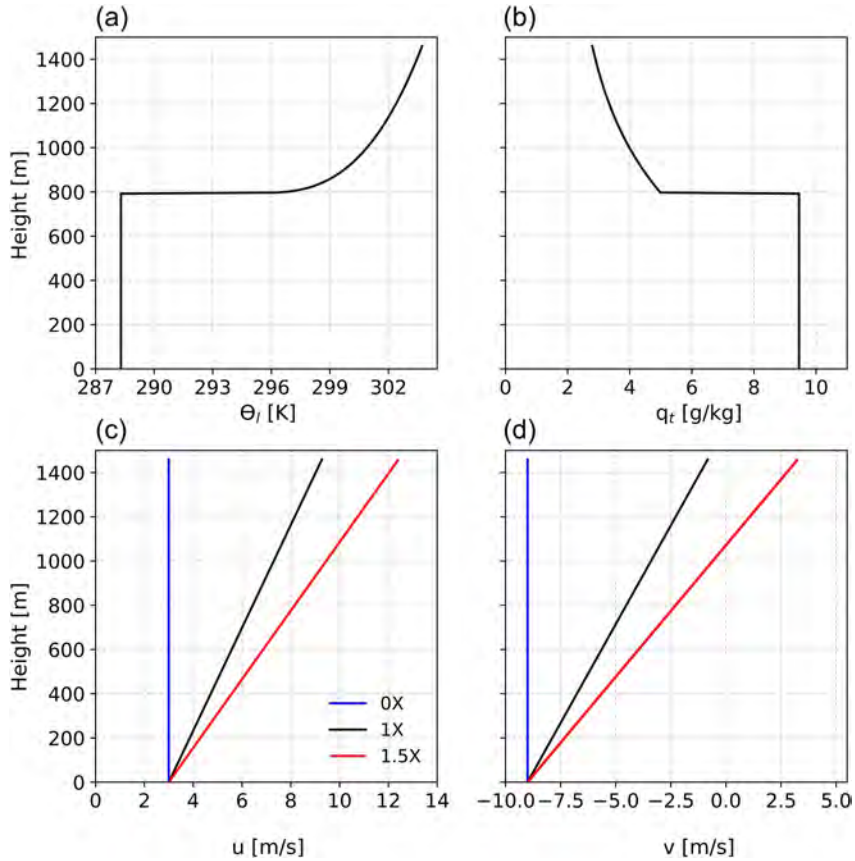


**Figure 1.** Initial profiles of (a) liquid-water potential temperature ($\theta_l$, K), (b) total water mixing ratio ($q_t$, g kg$^{-1}$), (c) $u$-wind (m s$^{-1}$), and (d) $v$-wind (m s$^{-1}$). Black profiles (1X) represent the standard GCSS values. Blue profiles (0X) stand for zero wind shear. Red profiles (1.5X) are 1.5 times the standard values.

the 1.5X $v$-wind changed the sign to northwesterly above ∼1.1 km (red line in Figure 1d), it does not affect the clouds because the initial inversion height is 795 m and the maximum cloud-top height remains below 900 m (discussed in Section 3.1). In all wind shear experiments (0X, 1X, and 1.5X), wind speed magnitude remained consistent with initial profiles at 3- and 6-hr into the simulation. However, horizontal winds ($u$ and $v$) exhibited a slight decrease below the inversion height (Figure S2 in Supporting Information S1). We experiment with different values of background prescribed $N_d = \{10, 35, 55\}$ cm$^{-3}$ (hereafter CDNC10, CDNC35, and CDNC55). We reduced the $N_d$ from the standard 55 cm$^{-3}$ because Savic-Jovcic and Stevens (2008) found that the standard $N_d$ produced too little surface precipitation compared to observations. In addition, Feingold et al. (2015) simulated the open-cell cloud by reducing the $N_d$ from 90 to 15 cm$^{-3}$.

### 2.3. Diagnostic of Cloud Organization

To fully account for the effects of cellular cloud organizations and structures, we characterize the cloud properties by using a cloud pseudo-albedo field to mimic those in satellite imagery. Although our simulations are nocturnal and we therefore do not consider shortwave radiation during the simulation, we can visualize and quantify the cloud field through the pseudo-albedo ($A$) with a good degree of approximation (i.e., cloud optical depth at a visible wavelength), which follows Zhang et al. (2005):

$$A = \frac{\tau}{6.8 + \tau} \tag{1}$$

where $\tau = 0.19\mathrm{LWP}^{5/6} N_d{}^{1/3}$ is the cloud optical depth, LWP is the liquid water path (vertical integral of liquid water), and $N_d$ is the prescribed value in the simulation. In the pseudo-albedo equation, the units of LWP and $N_d$ are kg m$^{-2}$ and kg$^{-1}$ ($10^3$ cm$^{-3}$), respectively.

Based on the cloud pseudo-albedo field, we classify and quantitatively evaluate the cloud spatial structures by using an object-based classification to measure the size and number of individual cloud segments in the domain. This approach is particularly useful for diagnosing different scales of cloud organization in LES experiments (Seifert & Heus, 2013). Cloud segments are identified from cloud mask fields when at least four cloudy pixels that neighbor each other horizontally are connected. We do not apply a smoothing or modification of the cloud pseudo-albedo field, because the results are not changed depending on the horizontal resolution (not shown, see Figure S1 in Janssens et al. (2021)). We only exclude clouds with pseudo-albedo <0.1, and small cloud segments (i.e., less than four cloudy pixels) were removed to avoid artifacts that were smaller than four times the grid resolution (Janssens et al., 2021).

### 2.4. Identification of Cold Pools

Three-dimensional buoyancy is calculated to identify the spatial structure of cold pools in the simulations. We take horizontal and vertical slices through the three-dimensional buoyancy field to analyze the interaction between cold pools and clouds. Following Tompkins (2001), the buoyancy ($b$; m s$^{-2}$) is defined as:

$$b = \frac{g\left(\theta_\rho - \overline{\theta_\rho}\right)}{\overline{\theta_\rho}} \tag{2}$$

where $g$ is the acceleration due to gravity, the overbar represents a horizontal domain mean, and $\theta_\rho$ is the density potential temperature ($K$) from Emanuel (1994), and is defined as:

$$\theta_\rho = \theta(1 + 0.608q_v - q_c - q_r) \tag{3}$$

where $\theta$ is potential temperature, and $q_v$, $q_c$, and $q_r$ are the mass mixing ratios of water vapor, cloud condensate, and rainwater, respectively. We identify cold-pool boundaries as the contour where $b$ first exceeds $-0.005$ m s$^{-2}$, following the threshold of Tompkins (2001). Cold-pool objects spanning fewer than 16 grid cells, with an equivalent diameter of ∼200 m at the lowest model height (2.5 m), are excluded. This criterion is the same as that applied to the cloud objects. For each column, we define the cold pool intensity ($B$; m s$^{-1}$) using the vertical integral of buoyancy following Bryan and Parker (2010) and Feng et al. (2015):

$$B = \sqrt{-2\int_0^h b\,dz} \tag{4}$$

where $b$ is buoyancy (Equation 2), and $h$ is the depth of the cold pool, defined as the height at which $b$ first exceeds $-0.005$ m s$^{-2}$ from the lowest model height to contiguous areas within identified the cold-pool object. The depth of cold pools in each column is then defined as the first vertical grid where the $b$ exceeds this threshold.

## 3. Results

### 3.1. Formation and Evolution of Cellular Cloud Structures

#### 3.1.1. Horizontal Structure of Cellular Clouds

The cloud structure and organization are characterized by the cloud pseudo-albedo field at the sixth hour of simulations in Figure 2. For each simulation, the cloud population had reached a stationary size distribution before the sixth simulated hour. Figure 2 shows that the clouds exhibit distinct spatial structures and morphological features as a function of $N_d$ (i.e., CDNC10, CDNC35, and CDNC55), and the vertical wind shear plays a minor role in cloud cellular organization. The cloud fields in CDNC10 appear in an open-cellular pattern, with clear regions surrounded by a "ring" of cloud (leftmost column in Figure 2). This open-cellular structure is characterized by highly reflective cell walls surrounding less reflective areas. The other $N_d$ experiments (CDNC35 and CDNC55) exhibit a closed-cellular pattern of cloudy regions surrounded by thin or cloud-free edges (middle and rightmost columns in Figure 2). The closed-cell structures are more uniformly distributed over the domain compared to the open-cell but are characterized by higher reflectivity at the cell centers. Cell walls are loci of low pseudo-albedo and in places may even be cloud-free. Interestingly, when the wind shear is increased (downward from the top

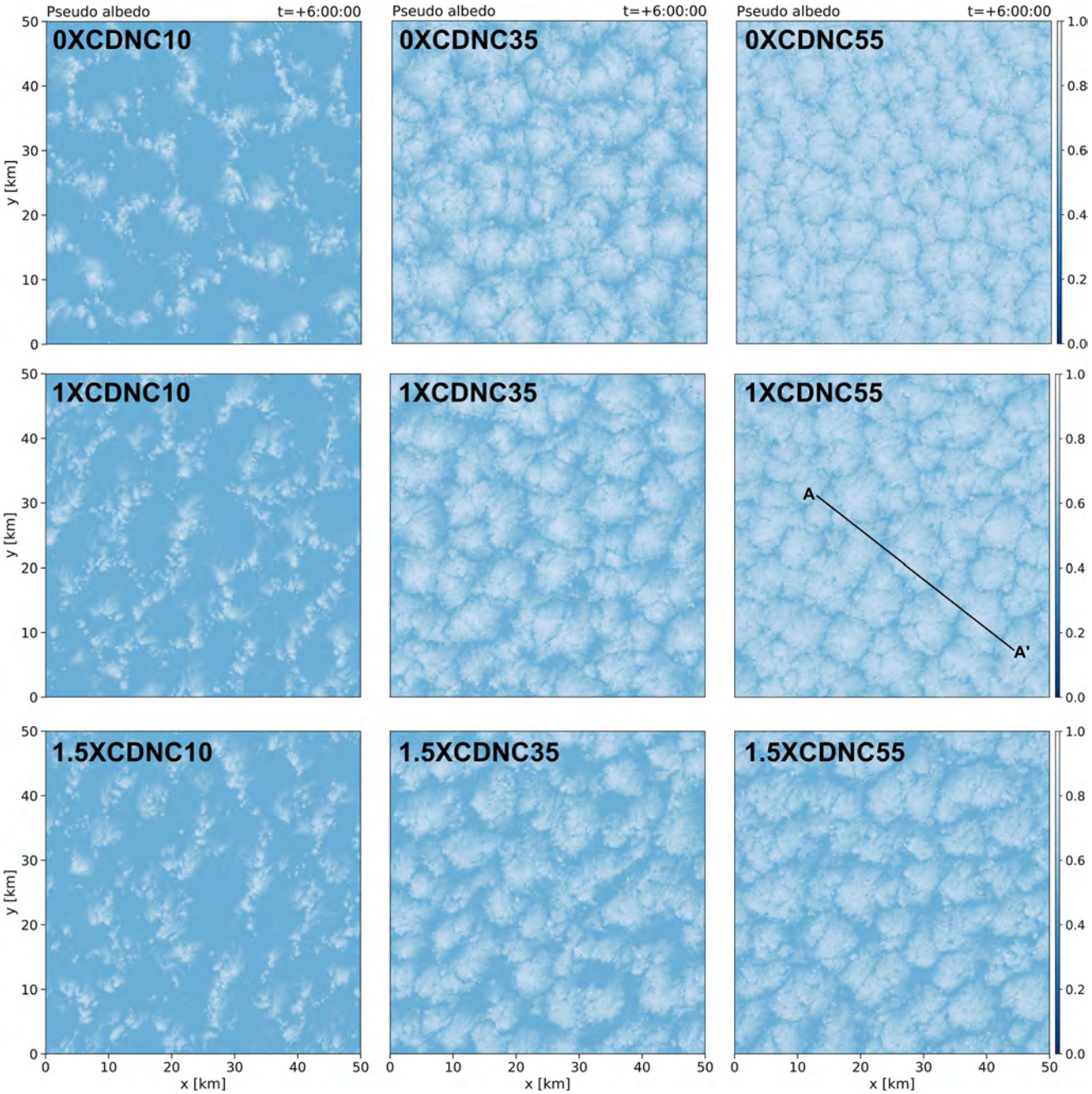


**Figure 2.** Snapshots of cloud pseudo-albedo fields at the sixth hour of simulations. Each column is for experiments CDNC10, CDNC35, and CDNC55 (corresponding to initial cloud droplet number concentrations of 10, 35, and 55 $cm^{-3}$, respectively). Each row is for wind shear experiments 0X, 1X, and 1.5X, representing the initial vertical wind profile multiplied by 0, 1, and 1.5, respectively. The line A–A′ indicates the location of the vertical cross-section used in Figure 3.

in Figure 2), both cloud types gradually reduce in size with more frequent breaks in cloudiness at cloud lateral edges. In addition, the closed-cell clouds in higher $N_d$ simulations exhibit more pronounced cloud-free regions with increasing wind shear. For low $N_d$ simulations, the open-cell clouds tend to elongate along shear and the aspect ratio increases with shear magnitude. We will quantitatively compare these characteristics in the next paragraph using object-based classifications.

### 3.1.2. Vertical Structure of Cellular Clouds

We further examine the cloud structures through a northwest-to-southeast oriented vertical cross-section along the direction of cloud propagation (i.e., line A–A′ in Figure 2). During the simulations, the clouds move southeastward

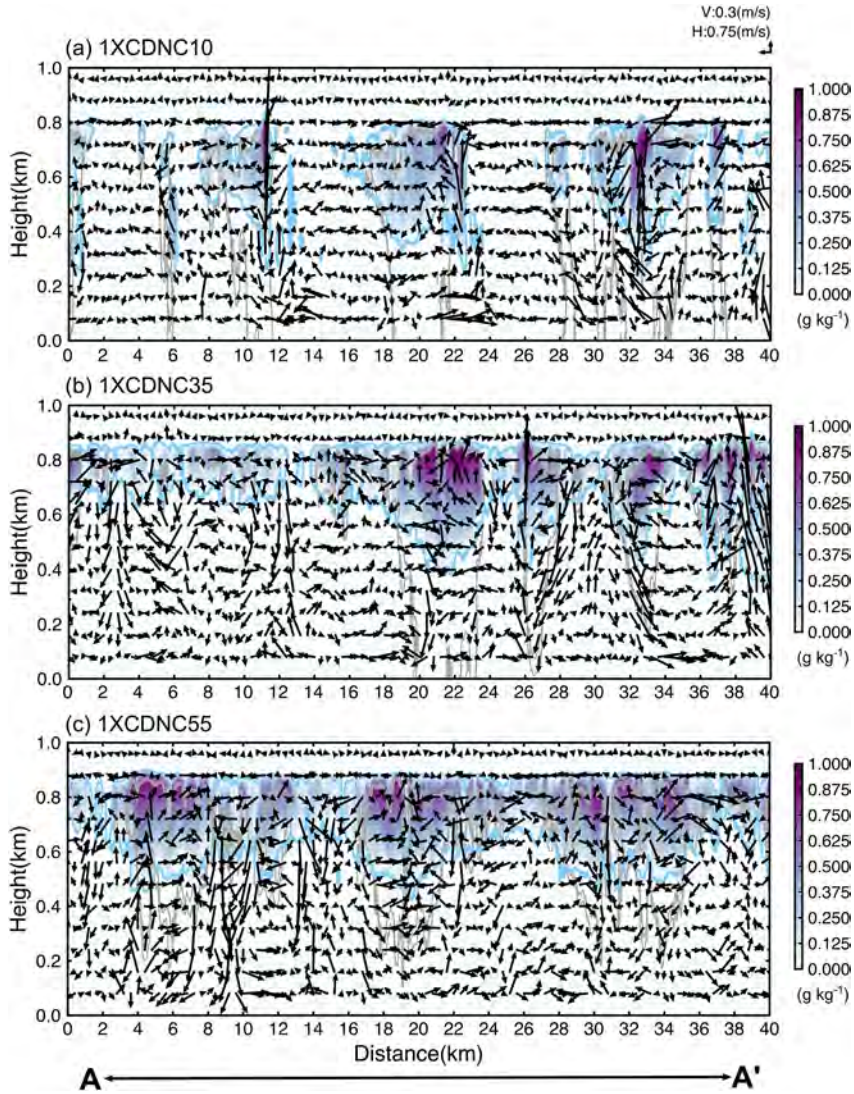


**Figure 3.** Vertical cross sections (transect A–A′ in Figure 2) of cloud water mixing ratio (>0.01 g kg$^{-1}$, shading colors), rainwater mixing ratio (>0.01 g kg$^{-1}$, gray dashed line), and winds (m s$^{-1}$, vector) along the section plane at the sixth hour of simulations from (a) 1XCDNC10, (b) 1XCDNC35, and (c) 1XCDNC55. Blue solid lines surround areas where cloud water mixing ratio exceeds 0.01 g kg$^{-1}$ and gray dashed lines surround areas where the rainwater mixing ratio exceeds 0.002 g kg$^{-1}$. The reference arrow for the vector magnitude is upper right.

with the environmental wind, even though the cloud propagation speeds are different depending on the background shear. Figure 3 shows the vertical structures of cellular clouds and circulation in the boundary layer as a function of $N_d$ for the standard (1X) vertical shear experiments. Results are similar for the 0X and 1.5X shear simulations, consistent with the finding that $N_d$ is the dominant factor for cellular cloud organization. As shown in the cloud pseudo-albedo fields, two distinct cloud structures are seen between 1XCDNC10 and the higher concentration simulations (1XCDNC35, 1XCDNC55). 1XCDNC10 shows a vertical structure of open cells characterized by spatially isolated precipitating cumuliform clouds. The clouds exhibit a narrow distribution of horizontal extent and a deeper cloud thickness compared with 1XCDNC35 and 1XCDNC55. The cloud top height reaches up to about 800 m, and cloud base extends down to about 400 m (Figure 3a). The upward motions are dominant close to downwind cloud lateral boundaries (e.g., $x$ = 12, 24 km) and downward motions in the clear atmosphere between cloudy cells (e.g., $x$ = 16, 26 km). Downdrafts below cloud base are also induced by precipitation loading (e.g., $x$ = 18, 30 km). This will be further discussed in Section 3.3. The vertical structure of open-cell clouds resembles that of shallow cumulus clouds observed using vertically pointing radar, as noted by Jeong et al. (2022). Their findings indicated that shallow cumulus clouds displayed a low cloud fraction with broken cloudy conditions.

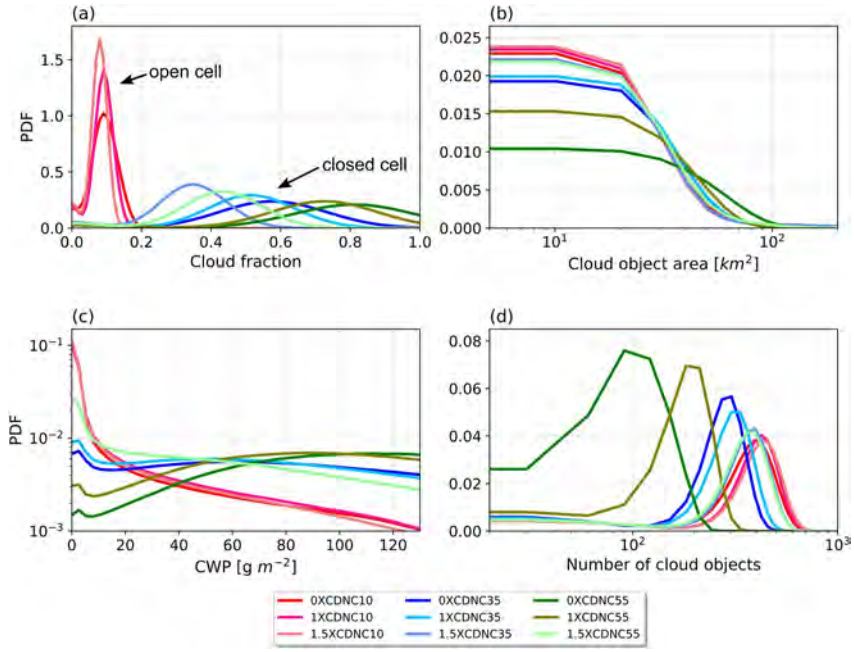


**Figure 4.** PDF of (a) cloud fraction, (b) cloud object area (km$^2$), (c) cloud water path (g m$^{-2}$), and (d) number of cloud objects during the simulation 3–12 hr after a spin-up period. Each experiment is presented with a different color, given in the legend below the panels.

The vertical structures of closed-cellular clouds (1XCDNC35 and 1XCDNC55) are shown in Figures 3b and 3c. The closed cells form relatively uniform cloud tops and cloud bases with large cloud fractions, which is also consistent with vertically pointing radar observations (Jeong et al., 2022). The cloud bases are lower in the presence of precipitation, for example, the cloud base heights in 1XCDNC35 are lower than 1XCDNC55. The averaged cloud-base heights in 1XCDNC35 and 1XCDNC55 are about 400 and 500 m, respectively. Most drizzle drops evaporate below the cloud base and there is very little surface precipitation in 1XCDNC55. Evaporation of drizzle drops below the cloud base cools and moistens the air in the closed-cellular clouds, leading to the formation of cold pools in the lower boundary layer and an important mechanism for open cell transitions (Feingold & McComiskey, 2016; Wang & Feingold, 2009a; Yamaguchi & Feingold, 2015). The vertical circulation patterns in both 1XCDNC35 and 1XCDNC55 are similar where strong updraft and downdraft locations are evident. The strong updrafts below the cloud base were dominant at the edge of cells around thinner cloud thickness (e.g., $x$ = 13, 30 km in 1XCDNC35, $x$ = 14–15, 26–27 km in 1XCDNC55), while the strong downdrafts are located at the center of cells, making a thicker cloud depth where drizzle and precipitation occur (e.g., $x$ = 20–22, 26 km in 1XCDNC35, $x$ = 5–7, 18–20 km in 1XCDNC55).

### 3.1.3. Cloud Spatial Structures Using Object-Based Classification

To quantitatively compare cloud cellular properties, we applied an object-based classification to measure individual cloud size and number across the simulations. Figure 4 shows probability density functions (PDF) of the following cloud properties over simulation hours 3–12 for all experiments: cloud fraction, cloud object area, cloud water path (CWP), and the number of cloud objects. Cloud object area is calculated from the number of grid columns within an identified cloud object. Cloud fraction is defined as the total cloud object area divided by the total number of horizontal grid cells. We then composited the cloud fraction every half hour during 3–12 hr of the simulation after the model spin-up period. The cloud fraction shows an apparent difference between open-cell clouds (e.g., CDNC10) and closed-cell clouds (e.g., CDNC35 and CDNC55) (Figure 4a). As shown above, the cloud pseudo-albedo and $q_c$ were very different across the $N_d$ experiments. Cloud fraction and cloud object area both tend to decrease with increasing wind shear (Figures 4a and 4b). Specifically, as wind shear increased, the cloud object areas in closed-cell clouds (CDNC35 and CDNC55) were highly reduced compared to those in open-cell clouds (CDNC10). Furthermore, there are many more small clouds under strong shear conditions, especially in the closed-cell clouds. For instance, in the strong wind shear experiment (1.5XCDNC55), there were a higher

portion of small clouds (<30 km$^2$) compared to 0XCDNC55 experiment (Figure 4b). This suggests that increasing wind shear leads to a decrease in the cloud amount through cloud thinning, in agreement with the surface and top wind shear experiments of Zamora Zapata et al. (2021). CWP also largely decreased in closed cells with stronger wind shear (Figure 4c). This means the vertical wind profiles affect the circulation and thermodynamic feedbacks on cloud water. We will further discuss the effects of wind shear on the cellular organization and cloud thinning in the next section. In contrast to cloud fraction and size, the closed-cell clouds have fewer cloud objects compared to the open-cell clouds (Figure 4d). This difference arises because closed-cell clouds are characterized by larger individual cloud object areas but a smaller overall number of cloud objects.

### 3.2. Effects of Wind Shear on Cloud Cellular Organization

In this section, we first examine the factors that determine why the simulations with stronger wind shear display lower cloud fraction than those with weaker shear. Figure 5 shows the time evolution of domain-averaged cloud properties, cloud base vertical velocity, and surface precipitation. As aforementioned, the different cloud morphological structures show distinct cloud fractions between open and closed cells as a function of $N_d$ (Figure 5a). In particular, the closed-cell clouds showed largely decreased CWP with increasing wind shear (Figure 5b). This is consistent with the PDF of cloud fraction (Figure 4a). Cloud fraction gradually decreases with time, and all simulations showed reduced cloud fraction with increasing wind shear. There are two possible factors associated with cloud thinning in the presence of strong wind shear. First, the entrainment mixing process leads to cloud thinning surrounding the cloud edge (Bretherton et al., 2007; Moeng, 2000; Stevens, 2002). The entrainment of dry and warm environmental air near the cloud top reduces LWP (known as evaporation-entrainment feedback; Jiang & Feingold, 2006; Xue & Feingold, 2006). Therefore, strong wind shear cases show largely reduced LWP (Figure 5c), and the clouds with increasing wind shear resulted in less cloud amount and more cloud breakup (Figure 2). The wind shear effect on LWP is more pronounced for closed cells than open cells. Second, strong wind shear leads to a deeper boundary layer and a more elevated cloud base. Averaged cloud top heights were not obviously different in wind shear experiments, but cloud base heights tend to increase with stronger wind shear (Figure 5d). The elevated cloud base in turn leads to cloud thinning. The elevated cloud base is also related to enhanced cloud-based updraft (Figure 5e). This increasing cloud-base updraft velocity can induce an increase in the cloud-top entrainment, which results in a more rapid evaporation rate and reinforces a reduction in LWP. Furthermore, open-cell clouds (CDNC10) show relatively high surface precipitation, while closed-cell clouds (CDNC35 and CDNC55) produce little to none (Figure 5f). While the higher concentration cases produce some drizzle at cloud base, most of it evaporates before reaching the surface as shown in Figures 3b and 3c.

We further examine the thermodynamic profiles to explain the entrainment associated with cloud thinning. For this reason, the domain averaged profiles of liquid water mixing ratio ($q_l$) and liquid water potential temperature ($\theta_l$) at 6 hr of the simulations are presented in Figure 6. The profiles of $q_l$ show that closed cells had a sharper inversion and higher inversion height than that of open cell cases (Figure 6a). There is more variability in simulations with differing $N_d$ than in simulations with differing shear. Stronger wind shear resulted in lower $q_l$ than weaker shear within the cloud layer, suggesting that stronger wind shear enhanced mixing of surrounding drier environmental air in the cloud layer. Furthermore, the closed-cell cases showed very low $q_l$ near the cloud base (~400 m), which is also related to entrainment causing faster evaporation for the higher $N_d$ experiments (Bretherton et al., 2007; Hill et al., 2009; Xue et al., 2008). The low $q_l$ is also related to the cloud base being elevated in closed-cell simulations (Figure 5d). The profiles of $\theta_l$ show a well-mixed environment for the CDNC35/55 simulations and a slightly stable profile for CDNC10 (Figure 6b). When we more closely examine the inversion layers in Figure 6c, strong wind shear cases have a weaker, more gradual inversion with higher inversion heights. This means that, in all simulations, the dilution across the inversion can reduce the cloud fraction as a result of increased mixing from above. The profiles of $\theta_l$ in the lower boundary layer (<400 m) show that strong wind shear cases have slightly more well-mixed structures than weak shear cases. Similarly, the closed-cell clouds show more coupled structures than open-cell clouds, because the evaporation of precipitation in the open cells leads to the cooling of the sub-cloud layer and decoupling of the boundary layer.

The analysis of the domain averaged profiles of the vertical velocity ($w$) variance ($\overline{w'w'}$) and the third moment of ($\overline{w'w'w'}$) at the sixth hour of the simulations is presented in Figures 7a and 7b. The closed cells show larger in-cloud $w$ variance in cloud layer compared with open cells (Figure 7a). The increased $w$ variance is related to radiative cooling, which produces a strong circulation at the cloud top via negative buoyancy. Additionally, the

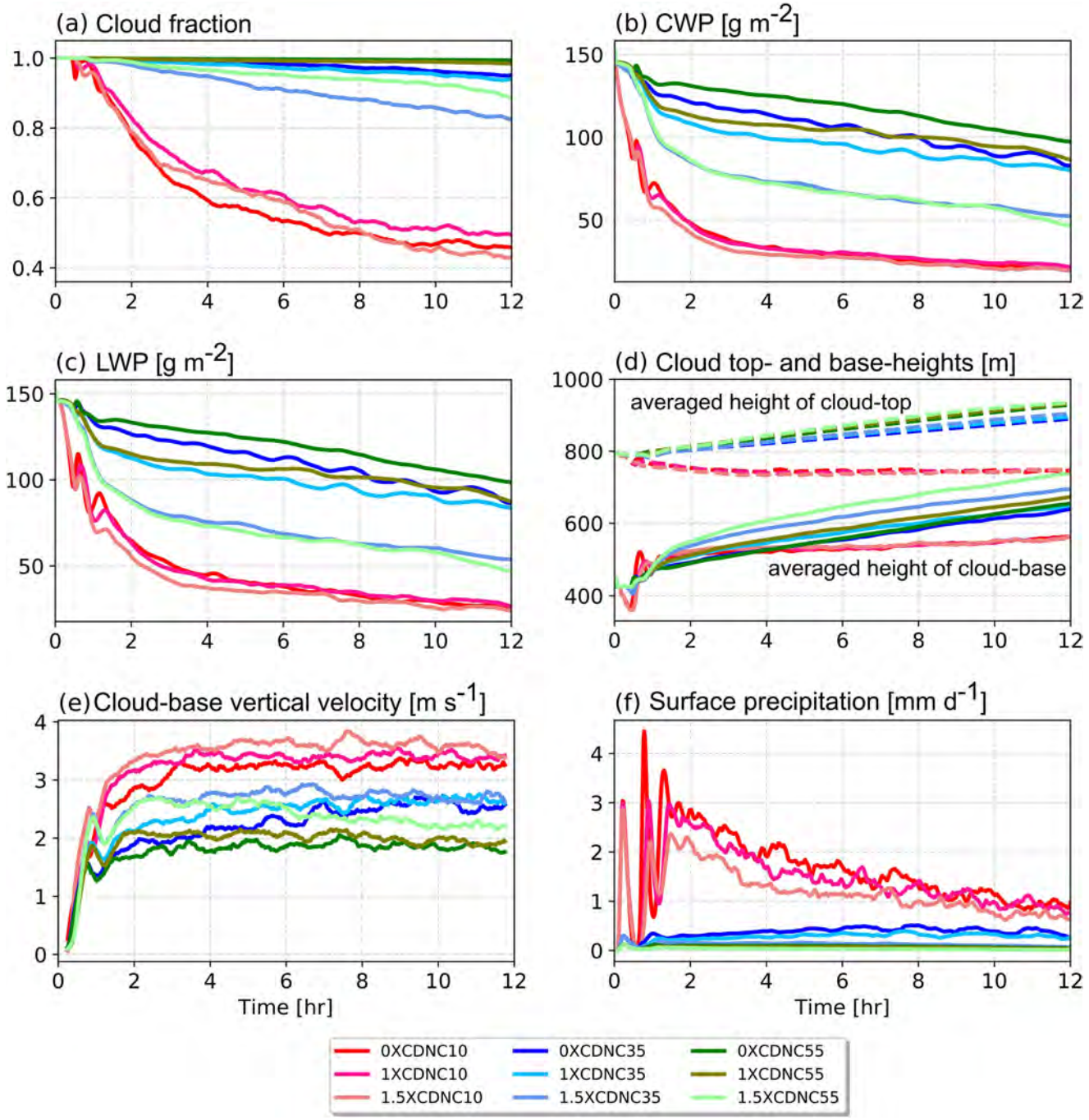


**Figure 5.** Time series of domain averaged (a) cloud fraction, (b) cloud water path (CWP, g $m^{-2}$), (c) liquid water path (LWP, g $m^{-2}$), (d) cloud boundaries (cloud top and base heights, m), (e) cloud-based vertical velocity (m $s^{-1}$), and (f) surface precipitation (mm $d^{-1}$) during the simulation hours.

differences between these two cloud types can be attributed to more intense precipitation in open-cell cases. This is because the cooling effect resulting from the evaporation of rain reduces the variance of vertical velocity. In these simulations, the maximum $w$ variance was located near the middle of the cloud layer, that is, at heights of approximately 550 m for open cells and 700 m for closed cells. Also, strong wind shear cases showed weaker $w$ variance in closed cells. Interestingly, 1.5X shear cases show a second peak of $w$ variance above the cloud top. These second peaks are representative of the substantial wind shear-induced turbulence across the inversion layer, which agrees with previous aircraft observations (Jen-La Plante et al., 2016; Malinowski et al., 2013) and wind shear LES simulation (Kopec et al., 2016). The $\overline{w'^3}$ profiles in all simulations are positive, and the maximum

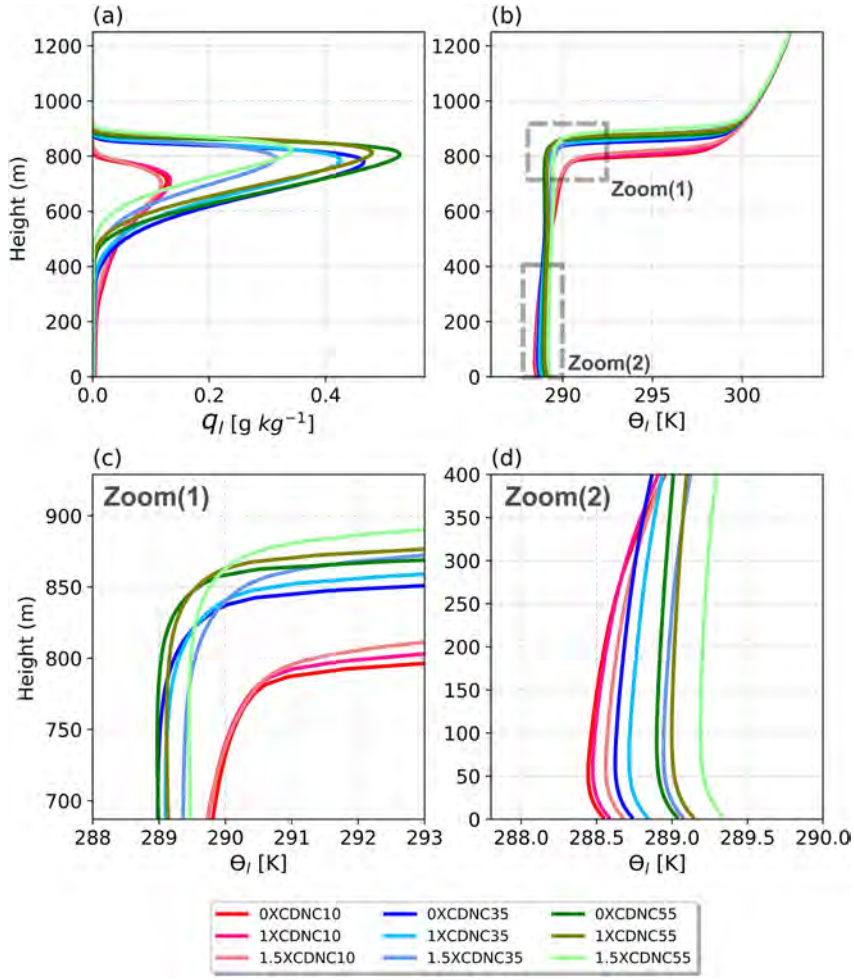


**Figure 6.** Vertical profiles of the domain averaged (a) liquid water mixing ratio ($q_l$, g $kg^{-1}$) and (b) liquid water potential temperature ($\theta_l$, K) with enlarged regions at (c) inversion region and (d) boundary layer at the sixth hour of simulations. Enlarged regions of the $\theta_l$ profiles are marked by dashed rectangles in (b).

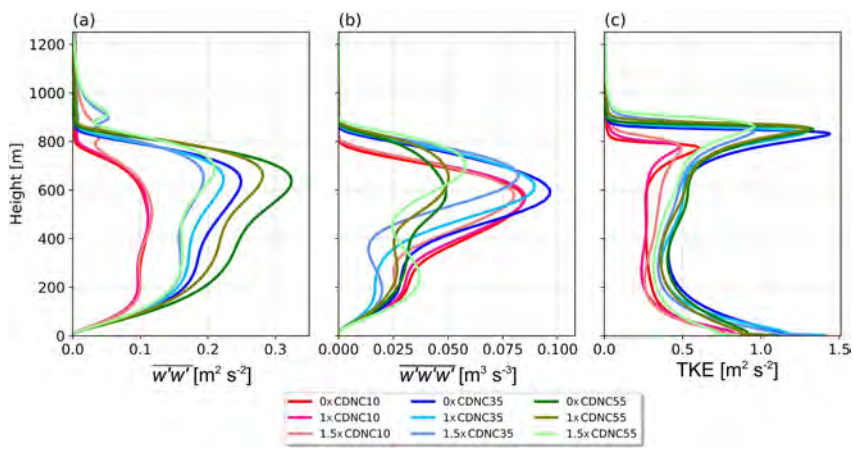


**Figure 7.** Vertical profiles of domain averaged (a) vertical velocity variance ($\overline{w'w'}$, $m^2$ $s^{-2}$), (b) third moment of vertical velocity ($\overline{w'w'w'}$, $m^3$ $s^{-3}$), and turbulent kinetic energy (TKE) ($m^2$ $s^{-2}$) at the sixth hour of simulations. An overbar represents a horizontal, spatial average, and a prime represents a deviation from that average.

$\overline{w'^3}$ was also located near the middle of the cloud layer, similar to $w$ variance (Figure 7b). The positive sign of $\overline{w'^3}$ throughout the profile for all simulations indicates radiative cooling (the nominal driver of cloud-top downdrafts) is a weaker source of turbulence than surface fluxes (which provide energy for surface-based updrafts), despite simulating a nocturnal case. In contrast with the $w$ variance, open cell clouds (CDNC10) have higher $\overline{w'^3}$ than the closed cell cases because strong vertical circulations are found in open cell walls (Figure 3a). Turbulent kinetic energy (TKE) profiles show peaks just above the inversion (Figure 7c) corresponding to shear-induced turbulence in the presence of strong static stability (hence no matching peak in the $\overline{w'^2}$ profiles). Strong shear cases tend to have weaker boundary layer TKE, especially in the closed cell simulations, because entrainment heating offsets the cloud top negative buoyancy induced by radiative cooling.

### 3.3. Cold Pool Interactions With Cloud Morphology

We now examine cold-pool strength and characteristics that depend on open- and closed-cell clouds under differing wind shear and cloud droplet concentration. Figure 8 shows near-surface buoyancy and identified cold-pool boundaries with negative buoyancy, as described in Section 2.4. The identified cold pools are characterized by relatively colder and drier air (see Figure S3 in Supporting Information S1) that have considerably lower moist static energy than the edge (Figure S4 in Supporting Information S1), in agreement with previous studies (de Szoeke et al., 2017; Feng et al., 2015). The CDNC10 simulations shows that stronger cold pools are associated with surface precipitation (leftmost column in Figure 8). Although the CDNC35 cases recorded a very small amount of surface precipitation (<0.1 mm $hr^{-1}$), they also produced large cold pools (middle column in Figure 8). The CDNC55 cases produced the smallest cold pools compared to other simulations with very little surface precipitation (rightmost column in Figure 8). This suggests that cold pools form without surface precipitation as long as there is a non-negligible drizzle flux at cloud base. We leave to future study the question of whether there exists a threshold drizzle flux for a given thermodynamic sounding at which cold pools begin to alter cloud field morphology. The spatial distributions of cold pools showed no significant differences when compared with the wind shear experiments. We will further elaborate on the impact of wind shear on cold pool characteristics in the next section.

We quantitatively compare the time evolution and PDFs of cold-pool depth, intensity, and temperature anomalies (deviation from the mean temperature over the domain) within the cold-pool boundaries in Figure 9. The cold-pool boundaries are indicated by black contours in Figure 8. Interestingly, the evolution of cold pool properties (depth and intensity) between CDNC10 and CDNC35 are similar (Figures 9a and 9b), even though the simulations have quite different surface precipitation intensities and surface temperature anomalies (Figures 5f and 9c). Previous studies suggest that cold-pool frequency and characteristics are closely related to surface precipitation (de Szoeke et al., 2017; Feng et al., 2015; Vogel et al., 2021) and that relatively stronger precipitating clouds produce longer-lasting, larger, deeper, and more intense cold pools. For the CDNC35 case, it is likely that cold pools are mainly driven by drizzle evaporation below the cloud base, and this evaporation is sufficient to prevent strong surface precipitation. We also aggregate these cold-pool characteristics during hours 6–12 of the simulations in mature cellular clouds. The shape of distributions of cold-pool properties (depth and intensity) between CDNC10 and CDNC35 also are similar (Figures 9d and 9e). However, CDNC10 simulations showed slightly deeper cold-pool depth and a larger cold-pool intensity compared to CDNC35. In addition, temperature anomalies in CDNC10 have longer tails (Figure 9c), suggesting that the magnitude of temperature depressions within cold-pool boundaries are strongly related to surface precipitation. These results are in agreement with previous findings using a long-term observational data set (Vogel et al., 2021). They classified the mesoscale cloud organization of trade wind cumulus into four dominant patterns (e.g., Sugar, Gravel, Flowers, and Fish) following Stevens et al. (2020), and found that cold-pool intensity and frequency were closely correlated with cloud organizational pattern.

The effect of wind shear on the cold-pool properties (depth and intensity) was less pronounced in all simulations. Specifically, the open cell clouds (CDNC10) showed very small differences with increasing wind shear, with an averaged cold-pool depth difference of −2.2 m and no obvious difference in cold-pool intensity between 0X and 1.5X. In the CDNC35 case, these differences were more noticeable than for CDNC10 and there were some changes among the wind shear experiments. For instance, the averaged cold-pool depth difference was 27.7 m, and cold-pool intensity showed a variance of 0.05 m $s^{-1}$. Wang and Feingold (2009a) also found slight differences in cloud albedo when the cloud field was stretched in the direction of the mean wind with increasing wind shear.

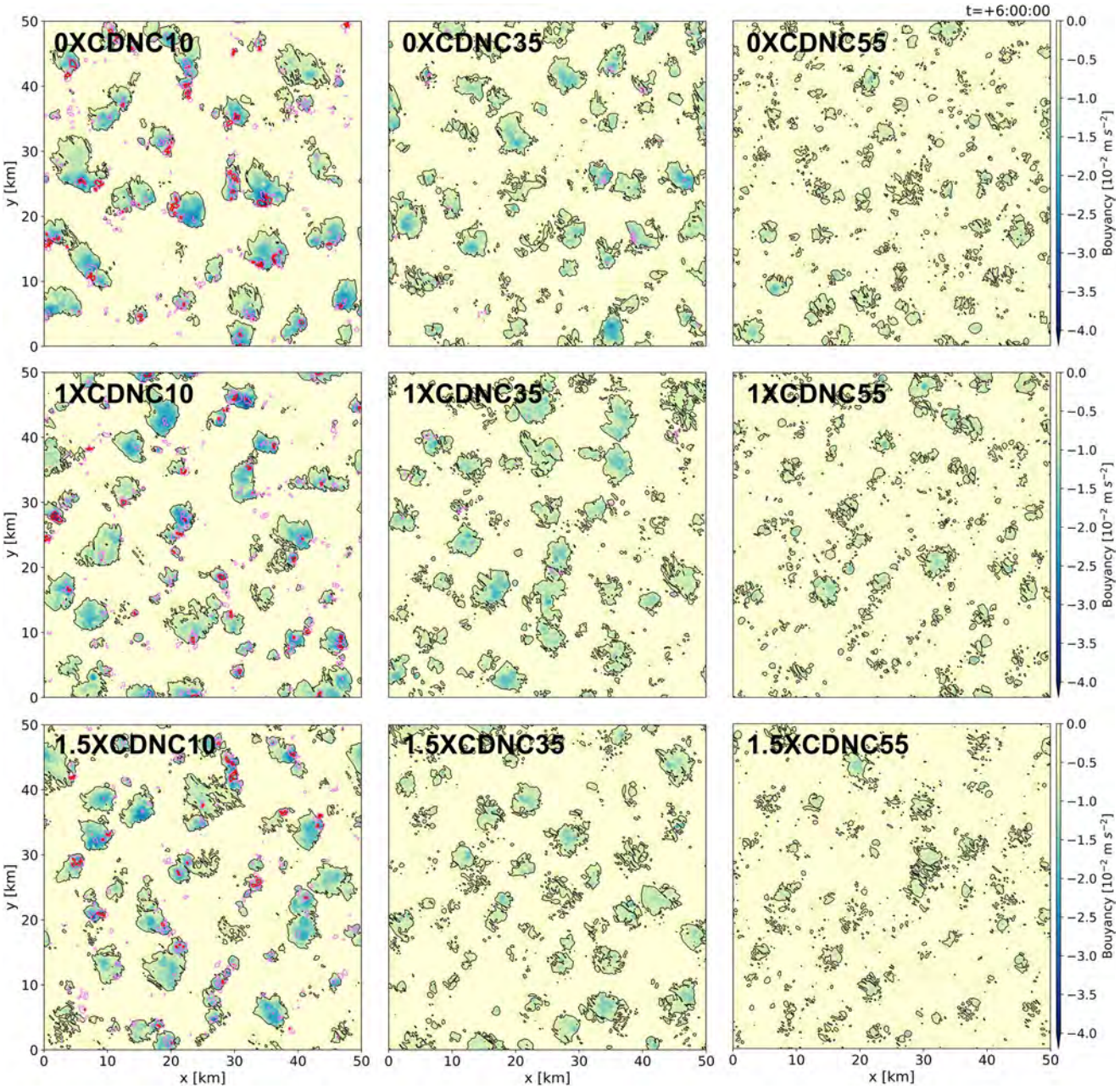


**Figure 8.** As in Figure 2, but for buoyancy fields (m $s^{-2}$, shading colors) at 2.5 m. The black contours correspond to the boundaries obtained using the method of Tompkins (2001) with a buoyancy threshold of −0.005 m $s^{-2}$. The red and violet contours indicate surface rain rate exceeding 1.0 and 0.1 mm $hr^{-1}$, respectively.

However, vertical velocity showed no notable changes in the wind shear experiments. Therefore, it appears that the wind shear does not significantly affect the cold-pool depth and intensity.

Figure 10 presents the divergence field (positive values indicate divergence, negative values convergence) at 10 m above the surface. The convergence and divergence fields are elongated in the direction of mean winds, resulting in an increase in the strength of convergence and divergence with higher wind shear. The cloud cellular structures were well represented in divergence fields, for example, individual open cells that were bordered by a strong divergence regime (leftmost column in Figure 10), where precipitation was produced in these ringlike structures (red and violet lines in Figure 8). This is because heavy drizzle coincides with a relatively strong downdraft associated with the sedimentation and evaporation of raindrops and results in strong divergence near the surface. The acceleration of these downdrafts by evaporative cooling is what produces cold pools. Furthermore, the cold-pool

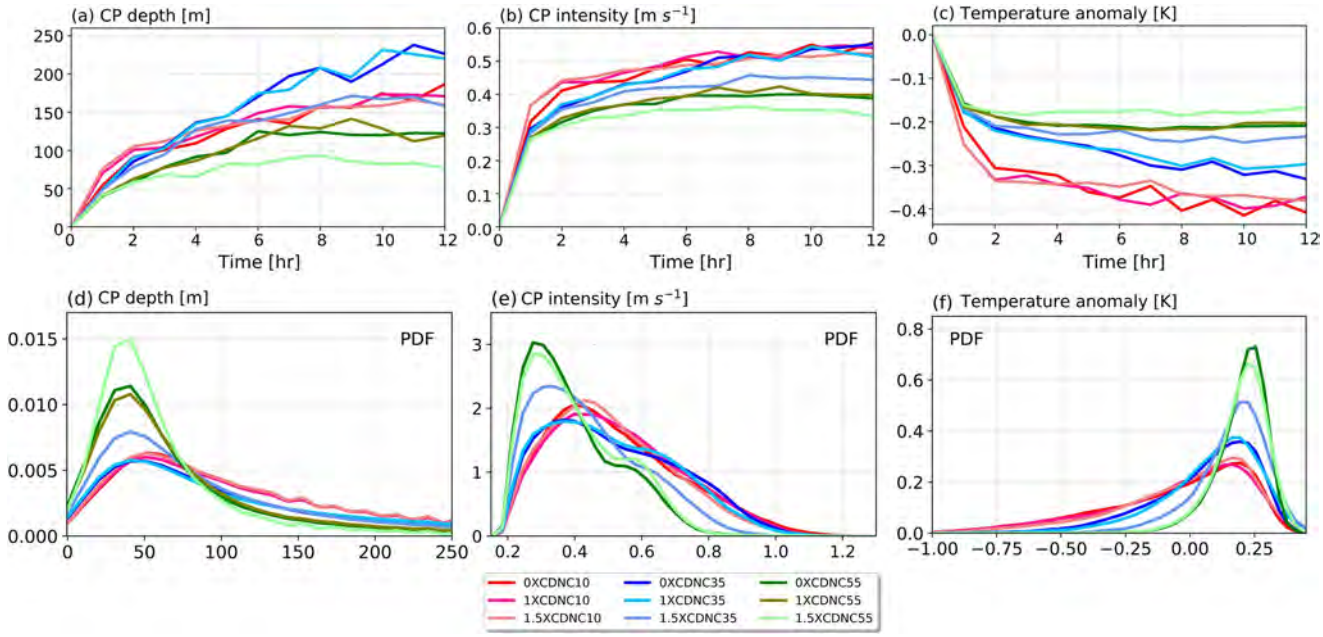


**Figure 9.** Time series of domain averaged (a) cold-pool depth (m), (b) cold-pool intensity (m s$^{-1}$), and (c) temperature anomaly (K). PDFs of (d) cold-pool depth, (e) cold-pool intensity, and (f) temperature anomaly for simulated hours 6–12.

boundaries coincide well with the locations of substantial convergence ($<-0.5 \times 10^3$ m$^{-1}$), suggesting relatively strong updrafts are promoted. The strong convergence is located near the southwest cold-pool boundary and the elongated pattern extending toward the southeast in 0XCDNC10 (Figure 11; enlarged area of $x$ = 27–37 km, $y$ = 1.5–11.5 km as a dashed box in Figure 10). The elongated convergence is due to the collision of outflow, and the position of this elongated convergence aligns with cold-pool boundaries (indicated by black contours in Figure 8). This result suggests that new convection can be triggered along the cold pool boundaries downstream of the cloud.

Figure 12 shows vertical cross sections (line B–B′ in Figure 10) along with precipitating and heavy drizzling cloud propagation in the same direction but zoomed in on the 6–32 km portion of the A-A′ transect illustrated in Figure 3. The open cell case (1XCDNC10) produces relatively strong precipitation and negative buoyancy related to rain evaporative cooling (e.g., cold pool generation) in the subcloud layer ($x$ = 10–15 km). The precipitating areas (violet contours) coincide with relatively strong downdrafts because downdrafts accelerate the sedimentation of raindrops. Downstream of the cloud ($x$ = 15–16 km), new convection is triggered as an updraft ascends over colliding outflow boundaries in the subcloud layer (Figure 12a). These updrafts occur in areas of convergence and cause clouds to form at the location of collision (Figure 13a). This suggests that cold pools play an important role in triggering new convection downstream through mechanical lifting (Feng et al., 2015; Jeong, Lee, & Wang, 2016; Jeong, Lee, Wang & Han, 2016; Zuidema et al., 2017). Furthermore, the initiation of subsequent convection can help maintain an open cellular structure and its associated updrafts and downdrafts.

Compared to 1XCDNC10, the convergence field resulting from the closed cell structure of 1XCDNC35 did not obviously lead to new convective initiation downstream, but the strong updrafts upstream of the region of the drizzle shaft ($x$ = 11–12 km) were elevated along the outflow boundary (Figure 12b). These forced uplifts may be enhanced by the collision of downdrafts ($x$ = 12–15 km) along the strong negative buoyancy related to drizzle evaporation. The cool air induced by evaporation of virga is negatively buoyant enough to sink down to the surface and spread out, forming a cold pool even when the rain does not survive to the surface. Also, the colliding air resulted in elevated convergence upstream of the drizzle shaft (Figure 13b).

1XCDNC55 showed relatively weak negative buoyancy ($x$ = 13–15 km) and smaller cold pools compared to 1XCDNC10 and 1XCDNC35. The reason for the small cold pools can be related to droplet sedimentation and entrainment feedback (Ackerman et al., 2004; Bretherton et al., 2007). These two previous studies proposed that droplet sedimentation was found to increase LWP by reducing the amount of cloud droplets near the cloud-top which are able to be affected by entrainment of dry free-tropospheric air from above. Similarly in 1XCDNC55,

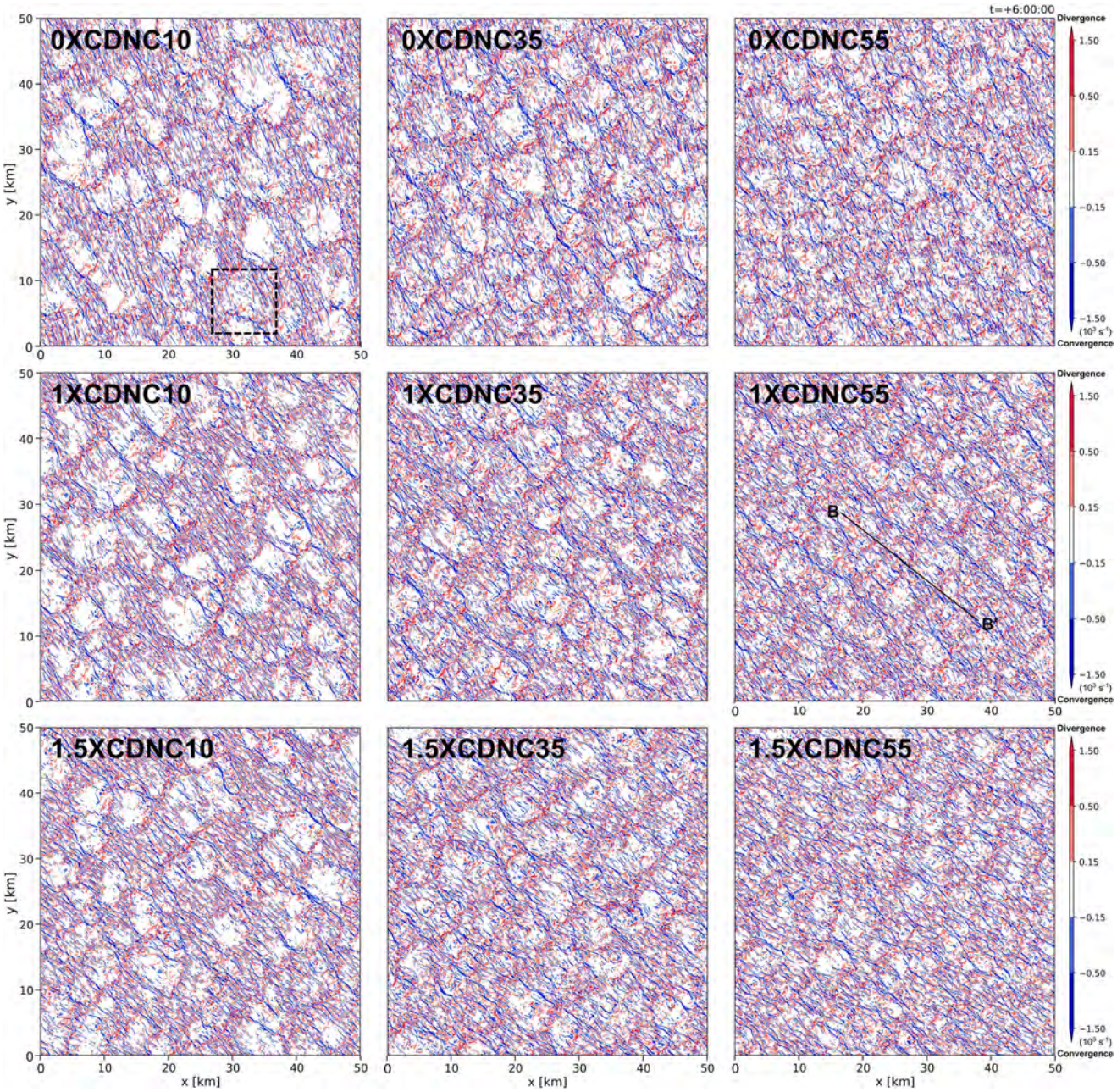


**Figure 10.** As in Figure 2, but for convergence and divergence fields ($\times 10^3$ s$^{-1}$, shading colors) at 10 m. The positive values represent divergence and negative values indicate convergence. The line B–B′ indicates the location of the vertical cross-section used in Figures 11 and 12. The black dashed box indicates the enlarged area for Figure 11.

higher $N_d$ decreases the mean droplet size and fall speed, making droplets more susceptible to the effects of entrainment at the cloud top. This causes reduced moisture available for evaporative cooling of downdrafts in the boundary layer due to the sinking of relatively warm and dry air from above the cloud top. Thus, the downdrafts below the cloud base were relatively weaker within regions of negative buoyancy ($x$ = 13–15 km) than in other experiments (Figure 12c), producing a weak divergence in this regime ($x$ = 12–16 km) (Figure 13c).

## 4. Summary and Conclusions

A series of large-eddy simulation (LES) experiments of nocturnal marine stratocumulus clouds are carried out based on DYCOMS-II RF02 (Ackerman et al., 2009). These simulations are used to investigate the effects of

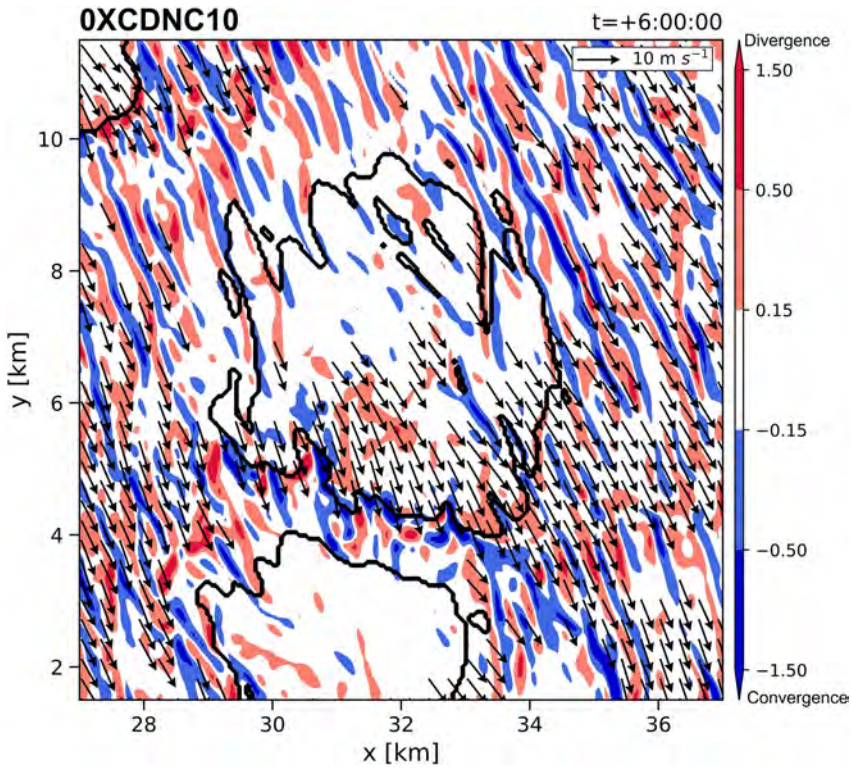


**Figure 11.** Snapshot of the convergence and divergence field ($\times 10^3$ s$^{-1}$, shading colors) in 0XCDNC10 at 6 hr of simulation. The positive values represent divergence and negative values indicate convergence. Black contours indicate cold-pool boundaries with a buoyancy threshold of −0.005 m s$^{-2}$. The arrows show 10 m winds (wind speeds >6.5 m s$^{-1}$).

wind shear and cloud droplet number concentration ($N_d$) as a proxy of aerosol loading on cellular cloud organization (e.g., open cells and closed cells) and cold pools. All nine experiments with different $N_d$ (10, 35, and 55 cm$^{-3}$) and wind shear profiles (0X, 1X, and 1.5X) are performed in a 50 × 50 km$^2$ domain for 12 hr using the three-dimensional CM1 model. The case simulated for this study is well-represented by a large horizontal domain when the low clouds are organized at the mesoscale by interactions among neighboring cells (de Roode et al., 2004). Simulated open and closed cloud cellular structures in vertical cross-sections (Figures 3 and 11) are remarkably consistent with radar observations (Jeong et al., 2022).

Our primary findings and discussions are summarized below by the schematic illustration in Figure 14. We find that $N_d$ is the dominant factor in determining cloud morphology (e.g., open vs. closed cells) for the DYCOMS-II RF02 case. Lower $N_d$ simulations (10 cm$^{-3}$; CDNC10) produce open cell structures (Figure 14a), and higher $N_d$ simulations (35 and 55 cm$^{-3}$; CDNC35 and CDNC55) produce closed cells (Figures 14b and 14c) regardless of the background vertical wind shear simulated. At least in the context of a highly idealized case study, we have shown that wind shear plays a minor role in formation of the open- and closed-cell cloud structure compared to $N_d$. The effects of wind shear on cloud properties are most easily seen in object-based cloud classification. All simulations showed a largely reduced cloud amount with increasing wind shear. The closed-cell clouds had a more profound wind shear effect on the cloud amount than open-cell clouds. The strong wind shear case showed cloud thinning for possible two reasons: (a) the entrainment of dry and warm environmental air near the cloud top reduced LWP and (b) the elevated cloud base resulted in the cloud thinning. The mixing of environmental air entrained through cloud top is shown by the purple vectors in Figures 14b and 14c.

Finally, we examined cold-pool characteristics of open- and closed-cell clouds. Open-cell clouds (e.g., 1XCDNC10) produce nontrivial surface precipitation with strong evaporative cooling near the surface (see blue shading in Figure 14a). The moderate $N_d$ closed-cell cloud configuration (e.g., 1XCDNC35) also produces frequent cold pools due to drizzle evaporation below the cloud base even though a very small amount of surface precipitation is produced (Figure 14b). This result differs from previous studies that suggest cold-pool strength and frequencies are closely related to surface rainfall intensity (de Szoeke et al., 2017; Feng et al., 2015; Vogel

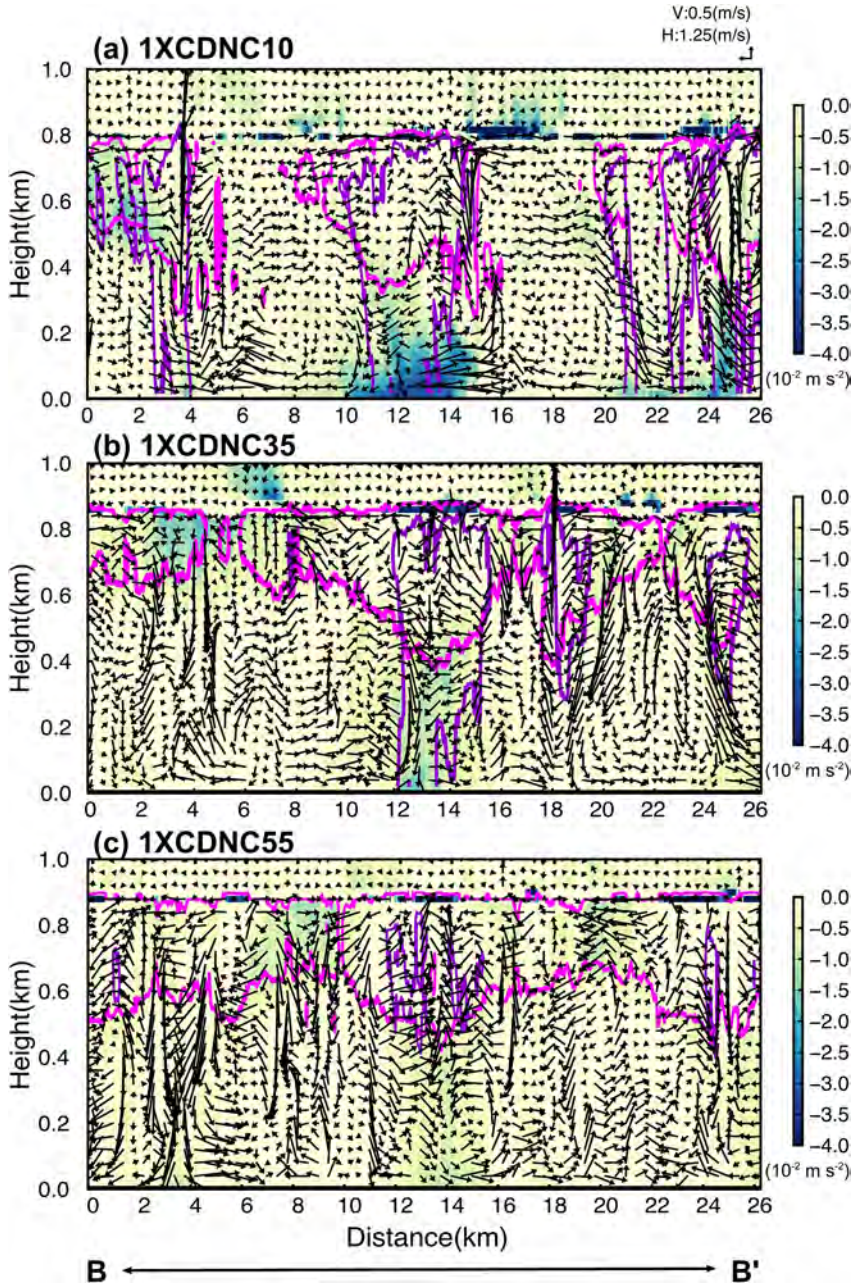


**Figure 12.** Vertical cross sections (transect B–B′ in Figure 10) of buoyancy (m $s^{-2}$, shading colors) along the section plane at the sixth hour of simulations from (a) 1XCDNC10, (b) 1XCDNC35, and (c) 1XCDNC35. Magenta lines are cloud water mixing ratio (>0.01 g $kg^{-1}$) and violet lines are rainwater mixing ratio (>0.01 g $kg^{-1}$). The reference arrow for wind (m $s^{-1}$, vector) magnitude is upper right.

et al., 2021). The strong surface precipitation produces larger, deeper, and longer-lasting cold pools. The highest $N_d$ experiments (i.e., 1XCDNC55) had the smallest cold-pool size and depth (Figure 14c). In addition, this study further discussed cold pool effects on open- and closed-cell clouds. For open-cell clouds, our simulations show new convection triggering over colliding outflow boundaries downstream of drizzle shafts, suggesting that cold pools play an important role in the initiation of subsequent convection (see secondary cell formation in Figure 14a). In the case of closed-cell clouds (1XCDNC35), our results reveal that elevated updrafts occur upstream of drizzle shafts along outflow boundaries, demonstrating that elevated updrafts promote closed-cell cloud organization. Closed-cell clouds (1XCDNC55) show relatively weak negative buoyancy compared with other simulations. This result can be related to the cloud and rain water sedimentation similar to those seen in

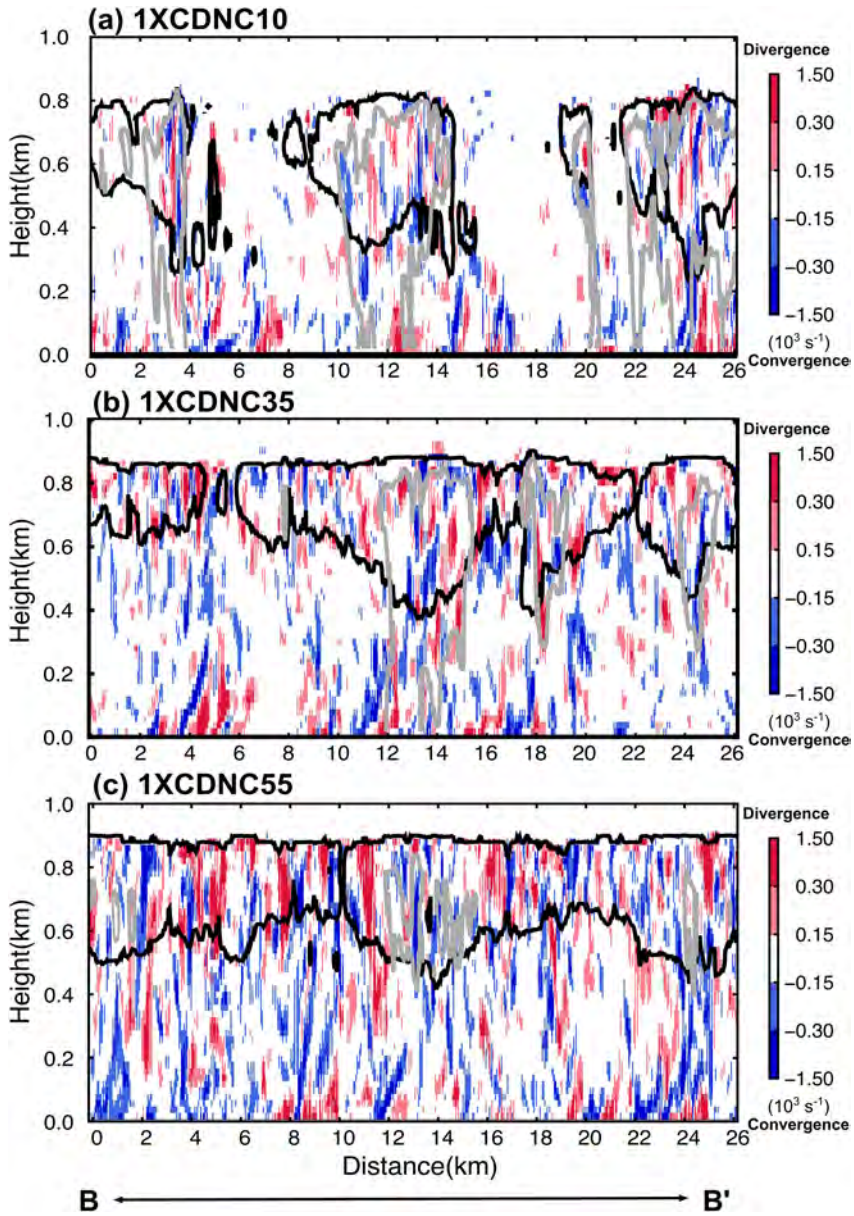


**Figure 13.** As in Figure 12, but for convergence and divergence fields ($\times 10^3$ s$^{-1}$). The positive values represent divergence and negative values indicate convergence. Black lines are cloud water mixing ratio (>0.01 g kg$^{-1}$) and gray lines are rainwater mixing ratio (>0.01 g kg$^{-1}$).

prior studies (Ackerman et al., 2004; Bretherton et al., 2007) and support the hypothesis that higher $N_d$ decreases cloud droplet size and fall speed with increasing cloud-top entrainment of dry air (purple vectors in Figure 14), which reduces the transport and amount of condensate available for evaporative cooling in the sub-cloud layer.

As a final note, this study aims to understand the wind shear and aerosol effects on open- and closed-cell clouds. As previously mentioned, it is apparent that wind shear has relatively less influence on the Sc cloud organization compared to $N_d$. This study is based on highly idealized LES experiments, and therefore, our conclusions are necessarily limited in scope. Consequently, the impact of wind shear on stratocumulus clouds may vary under different environmental conditions and within different types of stratocumulus cloud systems (e.g., in coupled vs. decoupled conditions).

Additionally, our findings show the significant role that cold pools play in secondary convection processes. The question is posed as to how cold pools affect the transition from open cells to closed cells or vice versa. Recent

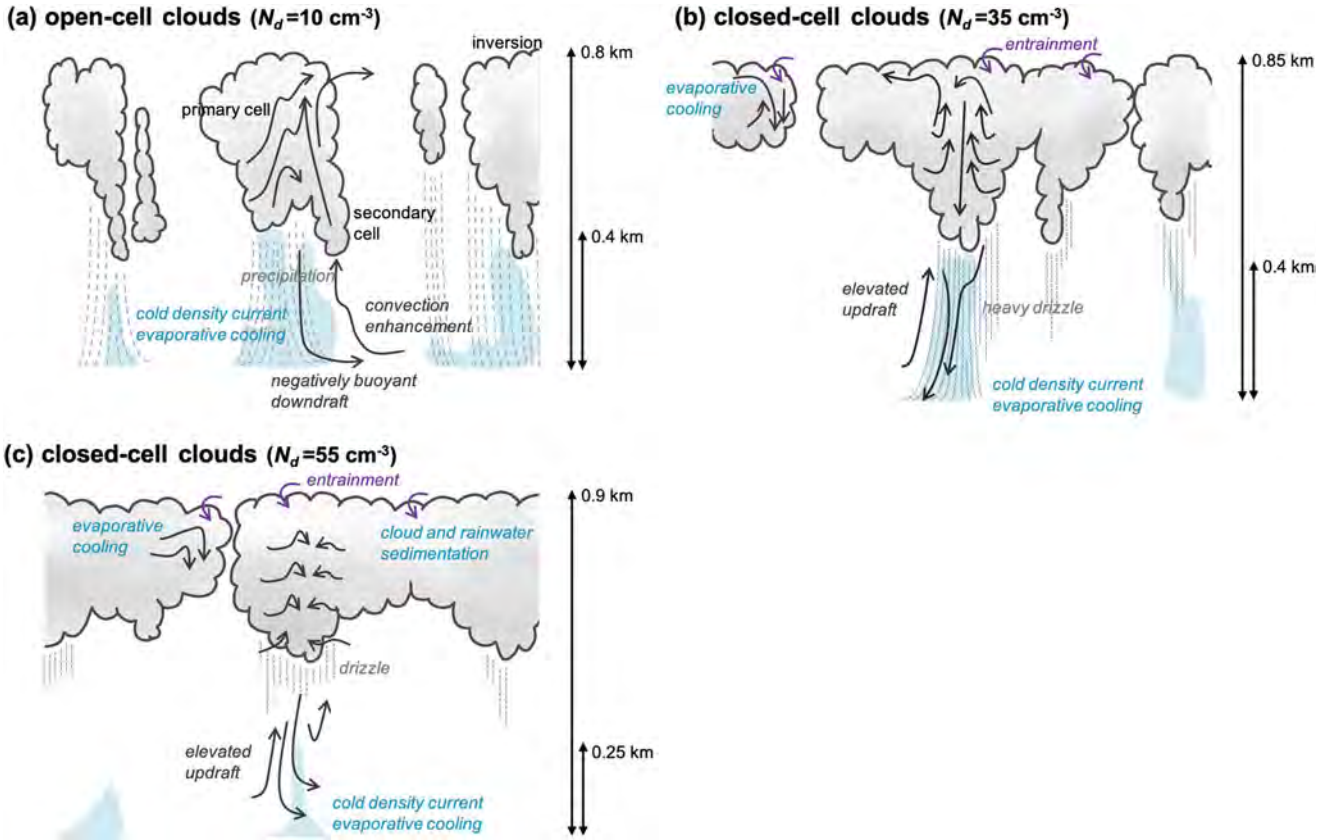


**Figure 14.** Schematic illustration depicting the effects of $N_d$ conditions in (a) 1XCDNC10, (b) 1XCDNC35, and (c) 1XCDNC55. The gray-shaded clouds represent stratocumulus clouds organized into open- and closed-cellular structures based on $N_d$ conditions. With increasing $N_d$, clouds represent as closed-cellular structures and cloud heights also increased, as indicated by black arrow to the right of each panel. Open-cell clouds (1XCDNC10) produced larger and deeper cold pools compared to closed-cell clouds (1XCDNC35 and 1XCDNC55). The cold pool played a role in initiating new convection and maintaining the cloud organization. Closed-cell clouds were significantly influenced by warm and dry air entrainment near the cloud-top. Additionally, negative buoyancy in the cloud region is related to cloud droplet sedimentation and evaporative cooling. Clouds in the illustration represent regions with cloud water mixing ratio greater than 0.01 g kg$^{-1}$. The light blue shading indicates the cold pool, identified by buoyancy exceeding −0.005 m s$^{-2}$.

studies examining the role of precipitation on transitions have taken the dynamical impact of subcloud evaporation as a given (e.g., Yamaguchi et al., 2017). In contrast, Kurowski et al. (2018) showed that the spatial heterogeneity of evaporation within rain shafts is critical for the shallow-to-deep convection transition; when the impacts of rain evaporation are horizontally homogenized, cold pool feedbacks are unable to reorganize boundary layer dynamics. Future study will examine cellular transitions in stratocumulus clouds and their interaction with cold pool dynamics using observation-based cases and LES simulations.

**Acknowledgments**
The authors thank the editor and three anonymous reviewers for their constructive and insightful comments on this study. This study was supported by the U.S. Department of Energy (DOE) Atmospheric System Research (ASR), an Office of Science Biological and Environmental Research program, under Grants DE-SC0020332 and DE-SC0022992. This study was also performed at the Jet Propulsion Laboratory, California Institute of Technology, under a contract with the National Aeronautics and Space Administration. This research used resources of the National Energy Research Scientific Computing Center (NERSC), a U.S. Department of Energy Office of Science User Facility operated under Contract DE-AC02-05CH11231.

## Data Availability Statement

The CM1 model is available from https://www2.mmm.ucar.edu/people/bryan/cm1/. The model setup follows the pre-configured namelist.input file (named as les_StratoCuDrizzle). Data (Jeong et al., 2023) used in the figures in this manuscript is available with a DOI of https://doi.org/10.5281/zenodo.7795949.

## References

Ackerman, A. S., Kirkpatrick, M. P., Stevens, D. E., & Toon, O. B. (2004). The impact of humidity above stratiform clouds on indirect aerosol climate forcing. *Nature*, *432*(7020), 1014–1017. https://doi.org/10.1038/nature03174

Ackerman, A. S., van Zanten, M. C., Stevens, B., Savic-Jovcic, V., Bretherton, C. S., Chlond, A., et al. (2009). Large-eddy simulations of a drizzling, stratocumulus-topped marine boundary layer. *Monthly Weather Review*, *137*(3), 1083–1110. https://doi.org/10.1175/2008MWR2582.1

Bony, S., & Dufresne, J.-L. (2005). Marine boundary layer clouds at the heart of tropical cloud feedback uncertainties in climate models. *Geophysical Research Letters*, *32*(20), L20806. https://doi.org/10.1029/2005GL023851

Bretherton, C. S., Blossey, P. N., & Uchida, J. (2007). Cloud droplet sedimentation, entrainment efficiency, and subtropical stratocumulus albedo. *Geophysical Research Letters*, *34*(3), L03813. https://doi.org/10.1029/2006GL027648

Bryan, G. H., & Fritsch, J. M. (2002). A benchmark simulation for moist nonhydrostatic numerical models. *Monthly Weather Review*, *130*(12), 2917–2928. https://doi.org/10.1175/1520-0493(2002)130<2917:ABSFMN>2.0.CO;2

Bryan, G. H., & Parker, M. D. (2010). Observations of a squall line and its near environment using high-frequency rawinsonde launches during VORTEX2. *Monthly Weather Review*, *138*(11), 4076–4097. https://doi.org/10.1175/2010MWR3359.1

Chakraborty, S., Fu, R., Massie, S. T., & Stephens, G. (2016). Relative influence of meteorological conditions and aerosols on the lifetime of mesoscale convective systems. *Proceedings of the National Academy of Sciences of the United States of America*, *113*(27), 7426–7431. https://doi.org/10.1073/pnas.1601935113

Chandrakar, K. K., Morrison, H., & Witte, M. (2022). Evolution of droplet size distributions during the transition of an ultraclean stratocumulus cloud system to open cell structure: An LES investigation using Lagrangian microphysics. *Geophysical Research Letters*, *49*(17), e2022GL100511. https://doi.org/10.1029/2022GL100511

Deardorff, J. W. (1980). Stratocumulus-capped mixed layers derived from a three-dimensional model. *Boundary-Layer Meteorology*, *18*(4), 495–527. https://doi.org/10.1007/BF00119502

de Roode, S. R., Duynkerke, P. G., & Jonker, H. J. J. (2004). Large-eddy simulation: How large is large enough? *Journal of the Atmospheric Sciences*, *61*(4), 403–421. https://doi.org/10.1175/1520-0469(2004)061<0403:LSHLIL>2.0.CO;2

de Szoeke, S. P., Skyllingstad, E. D., Zuidema, P., & Chandra, A. S. (2017). Cold pools and their influence on the tropical marine boundary layer. *Journal of the Atmospheric Sciences*, *74*(4), 1149–1168. https://doi.org/10.1175/JAS-D-16-0264.1

Emanuel, K. A. (1994). *Atmospheric convection*. Oxford University Press.

Fan, J., Yuan, T., Comstock, J. M., Ghan, S., Khain, A., Leung, L. R., et al. (2009). Dominant role by vertical wind shear in regulating aerosol effects on deep convective clouds. *Journal of Geophysical Research*, *114*(D22), D22206. https://doi.org/10.1029/2009JD012352

Feingold, G., Koren, I., Wang, H., Xue, H., & Brewer, W. A. (2010). Precipitation-generated oscillations in open cellular cloud fields. *Nature*, *466*(7308), 849–852. https://doi.org/10.1038/nature09314

Feingold, G., Koren, I., Yamaguchi, T., & Kazil, J. (2015). On the reversibility of transitions between closed and open cellular convection. *Atmospheric Chemistry and Physics*, *15*(13), 7351–7367. https://doi.org/10.5194/acp-15-7351-2015

Feingold, G., & McComiskey, A. (2016). ARM's aerosol–cloud–precipitation research (aerosol indirect effects). *Meteorological Monographs*, *57*, 221–2215. https://doi.org/10.1175/AMSMONOGRAPHS-D-15-0022.1

Feingold, G., McComiskey, A., Yamaguchi, T., Johnson, J. S., Carslaw, K. S., & Schmidt, K. S. (2016). New approaches to quantifying aerosol influence on the cloud radiative effect. *Proceedings of the National Academy of Sciences of the United States of America*, *113*(21), 5812–5819. https://doi.org/10.1073/pnas.1514035112

Feng, Z., Hagos, S., Rowe, A. K., Burleyson, C. D., Martini, M. N., & de Szoeke, S. P. (2015). Mechanisms of convective cloud organization by cold pools over tropical warm ocean during the AMIE/DYNAMO field campaign. *Journal of Advances in Modeling Earth Systems*, *7*(2), 357–381. https://doi.org/10.1002/2014MS000384

Ghan, S. J., Easter, R. C., Chapman, E. G., Abdul-Razzak, H., Zhang, Y., Leung, L. R., et al. (2001). A physically based estimate of radiative forcing by anthropogenic sulfate aerosol. *Journal of Geophysical Research*, *106*(D6), 5279–5293. https://doi.org/10.1029/2000JD900503

Glassmeier, F., & Feingold, G. (2017). Network approach to patterns in stratocumulus clouds. *Proceedings of the National Academy of Sciences of the United States of America*, *114*(40), 10578–10583. https://doi.org/10.1073/pnas.1706495114

Golaz, J.-C., Larson, V. E., & Cotton, W. R. (2002). A PDF-based model for boundary layer clouds. Part I: Method and model description. *Journal of the Atmospheric Sciences*, *59*(24), 3540–3551. https://doi.org/10.1175/1520-0469(2002)059<3540:APBMFB>2.0.CO;2

Hartmann, D. L., & Short, D. A. (1980). On the use of Earth radiation budget statistics for studies of clouds and climate. *Journal of the Atmospheric Sciences*, *37*(6), 1233–1250. https://doi.org/10.1175/1520-0469(1980)037<1233:OTUOER>2.0.CO;2

Helfer, K. C., Nuijens, L., de Roode, S. R., & Siebesma, A. P. (2020). How wind shear affects trade-wind cumulus convection. *Journal of Advances in Modeling Earth Systems*, *12*(12), e2020MS002183. https://doi.org/10.1029/2020MS002183

Hill, A. A., Feingold, G., & Jiang, H. (2009). The influence of entrainment and mixing assumption on aerosol–Cloud interactions in marine stratocumulus. *Journal of the Atmospheric Sciences*, *66*(5), 1450–1464. https://doi.org/10.1175/2008JAS2909.1

Houze, R. A. (2018). 100 years of research on mesoscale convective systems. *Meteorological Monographs*, *59*, 171–1754. https://doi.org/10.1175/AMSMONOGRAPHS-D-18-0001.1

Janssens, M., Vilà-Guerau de Arellano, J., Scheffer, M., Antonissen, C., Siebesma, A. P., & Glassmeier, F. (2021). Cloud patterns in the trades have four interpretable dimensions. *Geophysical Research Letters*, *48*(5), e2020GL091001. https://doi.org/10.1029/2020GL091001

Jen-La Plante, I., Ma, Y., Nurowska, K., Gerber, H., Khelif, D., Karpinska, K., et al. (2016). Physics of stratocumulus top (POST): Turbulence characteristics. *Atmospheric Chemistry and Physics*, *16*(15), 9711–9725. https://doi.org/10.5194/acp-16-9711-2016

Jeong, J.-H., Lee, D.-I., & Wang, C.-C. (2016). Impact of the cold pool on mesoscale convective system–produced extreme rainfall over southeastern South Korea: 7 July 2009. *Monthly Weather Review*, *144*(10), 3985–4006. https://doi.org/10.1175/MWR-D-16-0131.1

Jeong, J.-H., Lee, D.-I., Wang, C.-C., & Han, I.-S. (2016). Characteristics of mesoscale-convective-system-produced extreme rainfall over southeastern South Korea: 7~July~2009. *Natural Hazards and Earth System Sciences*, *16*(4), 927–939. https://doi.org/10.5194/nhess-16-927-2016

Jeong, J.-H., Witte, M., & Smalley, M. (2023). Effects of wind shear and aerosol conditions on the organization of precipitating marine stratocumulus clouds, April 3, 2023 release. https://doi.org/10.5281/zenodo.7795949

Jeong, J.-H., Witte, M. K., Glenn, I. B., Smalley, M., Lebsock, M. D., Lamer, K., & Zhu, Z. (2022). Distinct dynamical and structural properties of marine stratocumulus and shallow cumulus clouds in the eastern North Atlantic. *Journal of Geophysical Research: Atmospheres*, *127*(19), e2022JD037021. https://doi.org/10.1029/2022JD037021

Jiang, H., & Feingold, G. (2006). Effect of aerosol on warm convective clouds: Aerosol–cloud–surface flux feedbacks in a new coupled large eddy model.

Khain, A., Rosenfeld, D., & Pokrovsky, A. (2005). Aerosol impact on the dynamics and microphysics of deep convective clouds. *Quarterly Journal of the Royal Meteorological Society*, *131*(611), 2639–2663. https://doi.org/10.1256/qj.04.62

Khairoutdinov, M. F., & Kogan, Y. (2000). A new cloud physics parameterization in a large-eddy simulation model of marine stratocumulus. *Monthly Weather Review*, *128*(1), 229–243. https://doi.org/10.1175/1520-0493(2000)128<0229:ancppi>2.0.co;2

Klemp, J. B., & Wilhelmson, R. B. (1978). The simulation of three-dimensional convective storm dynamics. *Journal of the Atmospheric Sciences*, *35*(6), 1070–1095. https://doi.org/10.1175/1520-0469(1978)035<1070:tsotdc>2.0.co;2

Kopec, M. K., Malinowski, S. P., & Piotrowski, Z. P. (2016). Effects of wind shear and radiative cooling on the stratocumulus-topped boundary layer. *Quarterly Journal of the Royal Meteorological Society*, *142*(701), 3222–3233. https://doi.org/10.1002/qj.2903

Kurowski, M. J., Suselj, K., Grabowski, W. W., & Teixeira, J. (2018). Shallow-to-deep transition of continental moist convection: Cold pools, surface fluxes, and mesoscale organization. *Journal of the Atmospheric Sciences*, *75*(12), 4071–4090. https://doi.org/10.1175/JAS-D-18-0031.1

Li, Z., Niu, F., Fan, J., Liu, Y., Rosenfeld, D., & Ding, Y. (2011). Long-term impacts of aerosols on the vertical development of clouds and precipitation. *Nature Geoscience*, *4*(12), 888–894. https://doi.org/10.1038/ngeo1313

Malinowski, S. P., Gerber, H., Jen-La Plante, I., Kopec, M. K., Kumala, W., Nurowska, K., et al. (2013). Physics of stratocumulus top (POST): Turbulent mixing across capping inversion. *Atmospheric Chemistry and Physics*, *13*(24), 12171–12186. https://doi.org/10.5194/acp-13-12171-2013

Moeng, C.-H. (2000). Entrainment rate, cloud fraction, and liquid water path of PBL stratocumulus clouds. *Journal of the Atmospheric Sciences*, *57*(21), 3627–3643. https://doi.org/10.1175/1520-0469(2000)057<3627:ERCFAL>2.0.CO;2

Morrison, H., Curry, J. A., & Khvorostyanov, V. I. (2005). A new double-moment microphysics parameterization for application in cloud and climate models. Part I: Description. *Journal of the Atmospheric Sciences*, *62*(6), 1665–1677. https://doi.org/10.1175/JAS3446.1

Morrison, H., & Gettelman, A. (2008). A new two-moment bulk stratiform cloud microphysics scheme in the Community Atmosphere Model, Version 3 (CAM3). Part I: Description and numerical tests. *Journal of Climate*, *21*(15), 3642–3659. https://doi.org/10.1175/2008JCLI2105.1

Morrison, H., Thompson, G., & Tatarskii, V. (2009). Impact of cloud microphysics on the development of trailing stratiform precipitation in a simulated squall line: Comparison of one- and two-moment schemes. *Monthly Weather Review*, *137*(3), 991–1007. https://doi.org/10.1175/2008MWR2556.1

Orlanski, I. (1975). A rational subdivision of scales for atmospheric processes. *Bulletin of the American Meteorological Society*, *56*(5), 527–530. http://www.jstor.org/stable/26216020

Pawlowska, H., & Brenguier, J.-L. (2003). An observational study of drizzle formation in stratocumulus clouds for general circulation model (GCM) parameterizations. *Journal of Geophysical Research*, *108*(D15), 8630. https://doi.org/10.1029/2002JD002679

Peters, J. M., Morrison, H., Nelson, T. C., Marquis, J. N., Mulholland, J. P., & Nowotarski, C. J. (2022). The influence of shear on deep convection initiation. Part II: Simulations. *Journal of the Atmospheric Sciences*, *79*(6), 1691–1711. https://doi.org/10.1175/JAS-D-21-0144.1

Savic-Jovcic, V., & Stevens, B. (2008). The structure and mesoscale organization of precipitating stratocumulus. *Journal of the Atmospheric Sciences*, *65*(5), 1587–1605. https://doi.org/10.1175/2007JAS2456.1

Schneider, T., Teixeira, J., Bretherton, C. S., Brient, F., Pressel, K. G., Schär, C., & Siebesma, A. P. (2017). Climate goals and computing the future of clouds. *Nature Climate Change*, *7*(1), 3–5. https://doi.org/10.1038/nclimate3190

Seifert, A., & Heus, T. (2013). Large-eddy simulation of organized precipitating trade wind cumulus clouds. *Atmospheric Chemistry and Physics*, *13*(11), 5631–5645. https://doi.org/10.5194/acp-13-5631-2013

Seinfeld, J. H., Bretherton, C., Carslaw, K. S., Coe, H., DeMott, P. J., Dunlea, E. J., et al. (2016). Improving our fundamental understanding of the role of aerosol−cloud interactions in the climate system. *Proceedings of the National Academy of Sciences of the United States of America*, *113*(21), 5781–5790. https://doi.org/10.1073/pnas.1514043113

Shi, X., Hagan, H. L., Chow, F. K., Bryan, G. H., & Street, R. L. (2018). Large-eddy simulation of the stratocumulus-capped boundary layer with explicit filtering and reconstruction turbulence modeling. *Journal of the Atmospheric Sciences*, *75*(2), 611–637. https://doi.org/10.1175/JAS-D-17-0162.1

Siebesma, A. P., Soares, P. M. M., & Teixeira, J. (2007). A combined eddy-diffusivity mass-flux approach for the convective boundary layer. *Journal of the Atmospheric Sciences*, *64*(4), 1230–1248. https://doi.org/10.1175/JAS3888.1

Stevens, B. (2002). Entrainment in stratocumulus-topped mixed layers. *Quarterly Journal of the Royal Meteorological Society*, *128*(586), 2663–2690. https://doi.org/10.1256/qj.01.202

Stevens, B., Bony, S., Brogniez, H., Hentgen, L., Hohenegger, C., Kiemle, C., et al. (2020). Sugar, gravel, fish and flowers: Mesoscale cloud patterns in the trade winds. *Quarterly Journal of the Royal Meteorological Society*, *146*(726), 141–152. https://doi.org/10.1002/qj.3662

Stevens, B., & Feingold, G. (2009). Untangling aerosol effects on clouds and precipitation in a buffered system. *Nature*, *461*(7264), 607–613. https://doi.org/10.1038/nature08281

Stevens, B., Moeng, C.-H., Ackerman, A. S., Bretherton, C. S., Chlond, A., de Roode, S., et al. (2005). Evaluation of large-eddy simulations via observations of nocturnal marine stratocumulus. *Monthly Weather Review*, *133*(6), 1443–1462. https://doi.org/10.1175/MWR2930.1

Tompkins, A. M. (2001). Organization of tropical convection in low vertical wind shears: The role of cold pools. *Journal of the Atmospheric Sciences*, *58*(13), 1650–1672. https://doi.org/10.1175/1520-0469(2001)058<1650:OOTCIL>2.0.CO;2

van Zanten, M. C., & Stevens, B. (2005). Observations of the structure of heavily precipitating marine stratocumulus. *Journal of the Atmospheric Sciences*, *62*(12), 4327–4342. https://doi.org/10.1175/JAS3611.1

Vogel, R., Konow, H., Schulz, H., & Zuidema, P. (2021). A climatology of trade-wind cumulus cold pools and their link to mesoscale cloud organization. *Atmospheric Chemistry and Physics*, *21*(21), 16609–16630. https://doi.org/10.5194/acp-21-16609-2021

Wang, H., & Feingold, G. (2009a). Modeling mesoscale cellular structures and drizzle in marine stratocumulus. Part I: Impact of drizzle on the formation and evolution of open cells. *Journal of the Atmospheric Sciences*, *66*(11), 3237–3256. https://doi.org/10.1175/2009JAS3022.1

Wang, H., & Feingold, G. (2009b). Modeling mesoscale cellular structures and drizzle in marine stratocumulus. Part II: The microphysics and dynamics of the boundary region between open and closed cells. *Journal of the Atmospheric Sciences*, *66*(11), 3257–3275. https://doi.org/10.1175/2009JAS3120.1

Wicker, L. J., & Skamarock, W. C. (2002). Time-splitting methods for elastic models using forward time schemes. *Monthly Weather Review*, *130*(8), 2088–2097. https://doi.org/10.1175/1520-0493(2002)130<2088:TSMFEM>2.0.CO;2

Wood, R. (2005a). Drizzle in stratiform boundary layer clouds. Part I: Vertical and horizontal structure. *Journal of the Atmospheric Sciences*, *62*(9), 3011–3033. https://doi.org/10.1175/jas3529.1

Wood, R. (2005b). Drizzle in stratiform boundary layer clouds. Part II: Microphysical aspects. *Journal of the Atmospheric Sciences*, *62*(9), 3034–3050. https://doi.org/10.1175/jas3530.1

Wood, R. (2012). Stratocumulus clouds. *Monthly Weather Review*, *140*(8), 2373–2423. https://doi.org/10.1175/MWR-D-11-00121.1

Wood, R., & Hartmann, D. L. (2006). Spatial variability of liquid water path in marine low cloud: The importance of mesoscale cellular convection. *Journal of Climate*, *19*(9), 1748–1764. https://doi.org/10.1175/JCLI3702.1

Xue, H., & Feingold, G. (2006). Large-eddy simulations of trade wind cumuli: Investigation of aerosol indirect effects.

Xue, H., Feingold, G., & Stevens, B. (2008). Aerosol effects on clouds, precipitation, and the organization of shallow cumulus convection. *Journal of the Atmospheric Sciences*, *65*(2), 392–406. https://doi.org/10.1175/2007JAS2428.1

Yamaguchi, T., & Feingold, G. (2015). On the relationship between open cellular convective cloud patterns and the spatial distribution of precipitation. *Atmospheric Chemistry and Physics*, *15*(3), 1237–1251. https://doi.org/10.5194/acp-15-1237-2015

Yamaguchi, T., Feingold, G., & Kazil, J. (2017). Stratocumulus to cumulus transition by drizzle. *Journal of Advances in Modeling Earth Systems*, *9*(6), 2333–2349. https://doi.org/10.1002/2017MS001104

Yamaguchi, T., Feingold, G., & Kazil, J. (2019). Aerosol-cloud interactions in trade wind cumulus clouds and the role of vertical wind shear. *Journal of Geophysical Research: Atmospheres*, *124*(22), 12244–12261. https://doi.org/10.1029/2019JD031073

Zamora Zapata, M., Heus, T., & Kleissl, J. (2021). Effects of surface and top wind shear on the spatial organization of marine stratocumulus-topped boundary layers. *Journal of Geophysical Research: Atmospheres*, *126*(11), e2020JD034162. https://doi.org/10.1029/2020JD034162

Zhang, Y., Stevens, B., & Ghil, M. (2005). On the diurnal cycle and susceptibility to aerosol concentration in a stratocumulus-topped mixed layer. *Quarterly Journal of the Royal Meteorological Society*, *131*(608), 1567–1583. https://doi.org/10.1256/qj.04.103

Zhou, X., Heus, T., & Kollias, P. (2017). Influences of drizzle on stratocumulus cloudiness and organization. *Journal of Geophysical Research: Atmospheres*, *122*(13), 6989–7003. https://doi.org/10.1002/2017JD026641

Zuidema, P., Torri, G., Muller, C., & Chandra, A. (2017). A survey of precipitation-induced atmospheric cold pools over oceans and their interactions with the larger-scale environment. *Surveys in Geophysics*, *38*(6), 1283–1305. https://doi.org/10.1007/s10712-017-9447-x